國立交通大學

電子工程學系 電子研究所

博 士 論 文

鍺中三價受子和雙共振腔於兆赫波源之理論研究

Theoretical Studies of Group-III Acceptors in Germanium and Heterogeneous Cavities for Terahertz Emission

研 究 生：王德賢

指導教授：顏順通 教授

中 華 民 國 一 百 年 三 月

鍺中三價受子和雙共振腔於兆赫波源之理論研究

Theoretical Studies of Group-III Acceptors in Germanium and Heterogeneous Cavities for Terahertz Emission

研 究 生：王德賢　　Student：Te-Hsien Wang

指導教授：顏順通　　Advisor：Shun-Tung Yen

國 立 交 通 大 學

電子工程學系 電子研究所

博 士 論 文

A Dissertation
Submitted to Department of Electronics Engineering and
Institute of Electronics
College of Electrical and Computer Engineering
National Chiao Tung University
in partial Fulfillment of the Requirements
for the Degree of
Doctor of Philosophy
in
Electronics Engineering

March 2011
Hsinchu, Taiwan, Republic of China

中 華 民 國 一 百 年 三 月

鍺中三價受子和雙共振腔於兆赫波源之理論研究

學生王：王德賢　　指導教授：顏順通 博士

國立交通大學電子工程學系暨研究所

摘　　要

在本論文中我們分兩個部份分別討論兩種不同的半導體的兆赫波光源。第一個是摻雜三價受子的鍺。其可藉由電洞從鍺三價受子的激發態到基態的電隅極躍遷（electric-dipole transition）放出的兆赫頻段的電磁波。第二個是搭配兩種不同特性的共振腔所形成的拋物量子井雷射。我們預期在低溫下其可成為高功率的兆赫波光源。

在第一個部份中我們探討應力對鍺受子能階的電子結構（electronic structure）以及其電隅極躍遷的效應。而我們的計算是建立在等效質量理論（effective mass theory）並考慮了一個半經驗的雜質位能。這個雜質位能考慮了波向量 q 相關介電函數所造成的屏蔽效應以及中心核修正（central-cell correction）。

我們可以從受子態的成份來瞭解應力對電子結構和電隅極躍遷所造成的影響。在應力約小於 3 kbar 時受子態的束縛能會隨應力增加而快速地下降。此外我們發現偶對稱的受子態對於壓縮應力（compressive stress）和對伸張應力（tensile stress）展現出非對稱的特性。這是因為偶對稱的受子態重電洞（heavy-hole）和輕電洞（light-hole）的成份有很大的差異所造成。隨著應力的增加重電洞能帶和輕電洞能帶的隅合越來越小，且其在高應力（$\gtrsim$3 kbar）的情

況機乎可以乎略。此時受子態機乎是由單純的重電洞或是單純的由輕電洞所組成。這會造成受子態會有額外簡併的行為，且電隅極躍遷會有額外的選擇定則（selection rule）。我們針對低能量的激發態和基態間的躍遷在無應力和低應力（<0.35 kbar）的情況下做詳細的討論並且發現我們的結果與實驗比較達到定量的一致。至於高應力的情況目前並無實驗可供對照，我們也討論了理論模型在高應力下的適用性。

在第二個部份中我們提出並以理論証實一種雙共振腔的高功率的拋物量子井兆赫波雷射。當量子井與光子晶體-金屬-金屬共振腔共振時可以將載子次能帶間發光躍遷率（intersubband radiative transition rate）提高幾個數量級，而當量子井與法布利-培若（Fabry-Perot）共振腔產生共振會提高載子的帶間躍遷率（interband transition rate）。當這兩個共振腔同時與量子井共振，載子數和熱都會明顯地降低。此時，熱機乎不隨注入電流的增加而增加但兆赫波的發光強度卻可隨著注入電流呈線性地增加。我們預期這個系統可以有很好的發光效率且發光功率可輕易地達到 10 W/cm^2。

Theoretical Studies of Group-III Acceptors in Germanium and Heterogeneous Cavities for Terahertz Emission

Student：Te-Hsien Wang　　Advisors：Dr. Shun-Tung Yen

Department of Electronics Engineering & Institute of Electronics
National Chiao Tung University

ABSTRACT

In this dissertation, we study two types of semiconductor terahertz source. 1. The group-III acceptors in Ge under uniaxial stress. It can radiate terahertz electromagnetic wave through the electric-dipole transitions from the excited to the ground acceptor states. 2. The parabolic quantum wells laser with heterogeneous cavities. We expect it can be a high-power terahertz emitter.

In the first part of the dissertation, we study stress effect on the electronic structures and the electric-dipole transitions for group-III acceptors in Ge. The calculation is based on the effective mass theory with a semi-empirical impurity potential which considers the *q*-dependent screening and the central-cell correction. The stress effect on the electronic structures and the electric-dipole transitions can be undertood by connecting with the composition of the acceptor states. We find that the binding energies decrease rapidly with the stress in the low-stress region, and for even-parity states they exhibit remarkable asymmetry between the compressive and the tensile stress due to the large difference between the heavy-hole and the light-hole compositions. The coupling between the heavy-hole and the light-hole bands decreases with increasing stress and is almost negligible in the

high-stress region ($\gtrsim$ 3kbar). In this case, the acceptor states are almost pure heavy-hole or light-hole states. This causes the appearance of extra degeneracy of the acceptor states and additional selection rules of the electric-dipole transitions. In addition, we study in detail the electronic structures of the low-lying acceptor states and the electric-dipole transitions in the low-stress region. The results are in agreement with the currently available experimental data. However, because of the lack of the experimental data in the high-stress region, a justification is made for the applicability of our calculation for the case of high stress.

In the second part of the dissertation, we propose and demonstrate theoretically a scheme for high-efficiency terahertz lasing from parabolic quantum wells resonant coupled with two different cavities. An in-resonance photonic crystal metal-metal cavity can increase the intersubband radiative transition rates by several orders; an in-resonance Fabry-Perot cavity can increase the interband transition rate. Simultaneous interband and intersubband lasings can significantly reduce the carrier density and heat generation due to nonradiative processes. In this case, the heat generation remains low and constant, independent of the injection current but the terahertz emission power increases linearly with current. With the present scheme, terahertz emission power of 10 W/cm^2 can easily be achieved, accompanied by high intersubband quantum efficiency.

誌　　謝

首先我要感謝我的指導教授顏順通老師。他嚴謹認真的治學態度對我有深遠的影響。並且也感謝他在專業的領域上給我許多的指導和建議。我也要謝謝實驗室中相互提攜的同學們，特別是實驗室主要負責實驗的鐘佩鋼同學，因為他的研究領域與我相近，所以實驗相關的問題都可以與他討論。最後我將我最深的感恩獻給我的父母。謝謝他們在我求學過程中對我支持和鼓勵。

Contents

Table Captions

Chapter 1

Chapter 4

Figure Captions

Chapter 4

Chapter 5

Chapter 6

Chapter 1

Overview

Terahertz (THz) radiation is the electromagnetic (EM) wave whose frequency lies between the microwave and the infrared regions. The EM wave of 1 THz has a period of 1 ps, a wavelength of 300 μm, a photon energy of 4.1 meV, which divided by the Boltzmann's constant is a temperature of 47.6 K. There are many fundamental physics processes associated with the THz frequencies such as rotation of molecules, lattice vibrations, intraband transitions in semiconductors, and energy gaps of superconductors. Using the distinctive line structures of the various species of molecules, we can identify these molecules in an unknown material. In addition, we can obtain the information of the molecular collision by the line shapes of the spectrum. In the following section, we will describe the properties of THz radiation in different types of materials and the correlations between these properties and some interesting applications.

1.1 Properties and Applications of THz Radiation

According to the optical properties in the THz region, we can roughly divide common materials into three categories. The first one is metal, which has a high conductivity. Therefore, it is highly reflective in THz region. The second one is dielectric including, for instance, paper, clothes, wood, and plastic, etc. They have low conductivity and are almost nonpolar. They are usually opaque for visible light but transparent to THz EM waves. The third one is water. It is a strongly polar liquid, and is highly absorptive at THz frequencies. The properties of these materials as well as the semiconductor are given in Table 1.1. Since most of the materials for packaging are made of dielectric, which is transparent to THz EM waves, the THz imaging can be used to inspect the seal packages without causing any damage to the packages. Since water is highly absorptive in THz region, we can easily differentiate between the sub-

stances containing water and the dry materials. We can also easily identify the metal because it is highly reflective. Furthermore, we can combine spectral identification with imaging because many materials have unique spectrum in THz frequency. Because of the properties of THz EM wave mentioned above, the THz imaging has applications in many fields.

THz imaging can be applied to the problems of homeland security, because it can be used to identify illegal drugs, explosives, and weapons, concealed underneath most packaging materials, remotely. The other application is for earth and space science. By measuring the THz radiation from the atmosphere, we can monitor the atmospheric composition, and hence better understand the effect of ozone hole on the global warming. Furthermore, measuring the THz radiation from the outer space can help us to observe the birth of solar system and newborn galaxies as far as several billion light years away. This can be helpful to the investigation of the evolution of galaxies and the formation of stars and planets. THz radiation is also useful for biology and medical science and agriculture because of three reasons. The first is that most of the collective vibrational modes of protein and DNA lie in the THz region. The second is that THz radiation is very sensitive to water. This is useful because the small change of water content may represent crucial defects in the tissue. The third is that THz has much low photon energy in comparison with X-rays. Therefore, THz imaging will not cause damage to the tissues. Furthermore, THz radiation can be used for three dimensional imaging of teeth. The image can be more accurate than that obtained by X-ray imaging.

The study of THz radiation is growing in many independent fields. Here, we have just briefly described some applications in homeland security, earth and space science, biology and medical science and agriculture. THz radiation has many other applications. Readers can find the details from the review articles [1-7].

Table 1.1 Optical properties of different types of materials in the THz region.

Material Type	Optical Properties	Values at 1 THz
Liquid water	High absorption coefficient	$\approx$250 cm^{-1}
Metal	High reflectivity	>99.5 %
Plastic	Low absorption coefficient	<0.5 cm^{-1}
	Low refractive index	$\approx$1.5
Semiconductor	Low absorption coefficient	<1cm^{-1}
	High refractive index	~3-4

1.2 Terahertz Sources

Even though THz radiation has so many applications as mentioned in the previous section, the THz EM spectrum is the least explored region to date mainly due to the lack of compact, efficient, and cheap THz sources. This is why the region of THz EM spectrum is called the "THz gap". In the last two decades, there has been a dramatic increase in the number of publications on THz sources. In this section, we briefly describe the THz sources of different operation principles. The details can be found in the reviews [1-2, 4-7].

THz radiation can be generated through nonlinear crystals such as ZnTe, CdTe, and GaP. When two optical photons at frequencies ω_1 and ω_2 are incident upon the nonlinear crystal, the frequency of the output photon can be the difference between the two input frequencies $\omega_T = \omega_1 - \omega_2$. If the input light source is a femtosecond laser generating pulses of broad-band spectrum with bandwidth about 10 THz, the output is a broad-band THz pulses generated through optical rectification; If the input light source consist of two continuous wave (CW) optical beams with frequency difference in the THz region, the output is CW THz radiation generated through the difference frequency conversion (DFG). The optical-to-THz conversion efficiency of the nonlinear crystal has an upper limit determined by the Manley-Rowe relations. The upper limit is $n_o\omega_T / n_T(\omega_1 + \omega_2)$, and of the order of 10^{-3}~10^{-2}. Here, n_o and n_T are, respectively, the refractive indices in the optical and THz regions.

THz radiation can be generated through time-varying current in a biased photoconductive antenna. The photoconductive antenna has two metal electrodes on a semiconductor substrate. When the optical EM wave is incident upon the gap between the electrodes, the photocarriers are generated and can be accelerated by a static electric field. This results in a photocurrent varying with the intensity of the incident EM wave. Therefore, similar to the case of nonlinear crystals, the femtosecond laser pulses can generate a broad-band THz pulses and the two CW optical beams with frequency difference in the THz region can generate CW THz radiation.

THz radiation can be generated from accelerated electrons in vacuum. Backward wave oscillators (BWOs) and free-electron lasers (FELs) are two examples. The BWOs are vacuum tubes. The accelerated electrons in the vacuum tube interact with the EM modes of a metal grating. The metal grating is called a slow-wave structure because the accelerated electrons slow down when they go through the slow-wave structure. The kinetic energy of the electrons is transferred to EM energy through exciting the EM modes of the metal grating. The device is called BWO because the motion of the electrons and the group velocity of the EM waves are oriented in opposite directions. The output power of the BWO can be 100 mW below 0.2 THz but decreases rapidly with frequency (about 1 mW at 1 THz). In FELs, a relativistic electron beam passes through periodically alternating magnetic structure. The periodic magnetic field forces the electrons oscillating and hence radiate coherent EM wave. The FELs can reach high power and are the widest tunable laser. The range in wavelength is from microwaves to X-rays. However, the FELs are expensive and need a huge space.

THz radiation can be generated through radiative transitions between two energy levels. Far-infrared gas lasers, quantum cascade lasers (QCLs), and *p*-Ge lasers are three examples. The far-infrared gas lasers radiate photons through the transitions between the molecular rotation energy levels. The gain media are molecular gas such as CH_3Cl, CH_2F_2, NH_3, and CH_3OH. These molecules have permanent dipole moment. Therefore, they can couple the EM radiation. The far-infrared gas lasers have the advantages of high power and room-temperature operation. However, their frequencies are discrete and determined by the molecular rotational levels. Extra space is required for the cavity to confine the laser modes. In addition, some species of gas are toxic, and a high-voltage system is required.

The QCL and *p*-Ge laser are semiconductor THz sources, which have advantages such as compact, easily integrated, and low power consumption. A QCL consist of a repeated multiple quantum well heterostructures. Unlike the conventional semiconductor diode laser emit-

ting EM waves through the electron-hole recombination across the band gap, the QCL is unipolar and lasing through the radiative intersubband (ISB) transitions of electrons. After the ISB transition of the electron, the electron is at a lower subband and then injected to the next period to undergo another ISB transition. The repeating process is the origin of the name "cascade". One difficulty of the QCLs is that the electron distribution can easily affected by the thermal excitation because of the small separation between the subbands. The output power can be up to 100 mW at liquid temperature but decrease rapidly with increasing temperature. To date, room-temperature operation THz QCL is not available. Another problem of QCLs is the mode confinement. The conventional dielectric waveguide is not suitable because the decay length of the THz evanescent waves is much larger than the thickness of the active region. Semi-insulating surface plasma and metal-metal (MM) waveguides are two common solutions [8].

The *p*-Ge lasers generate THz radiation through the radiative transitions of holes from the long-lifetime light-hole (LH) to the heavy-hole (HH) Landau levels. Similar to the QCLs, thermal excitation is a problem. The lasing of *p*-Ge lasers requires the specific conditions of the applied crossed electric and magnetic fields. The frequency is continuously tunable from one to four THz by varying the strengths of the electric and the magnetic fields. THz radiation can also be generated through the radiative transitions between the acceptor levels in *p*-Ge. Contrary to the radiation through the hole transitions between Landau levels, that through the transitions between the acceptor levels do not require the applied magnetic field. The THz stimulated emission has been observed in the *p*-Ge in the presence of a uniaxial stress. The frequency is also continuously tunable by changing the applied stress [9].

1.3 **Contributions**

In the present dissertation, we study the group-III acceptors in strained Ge. As mentioned in the previous section, the THz emission can be obtained through the transitions of holes

between the acceptor states. In addition to the bulk *p*-Ge, we also study the effect of THz cavities on a parabolic quantum well (PQW) structure. We propose a high-power THz laser device with heterogeneous cavities. The main contributions of the present dissertation are listed as follows:

1. We calculate the electronic structure of acceptor states and the oscillator strengths of the electric-dipole transitions from the ground states for various group-III acceptors in Ge in the absence and presence of an uniaxial stress along the [001] direction.
2. Our results, including energy levels of acceptor states, the chemical shifts, and the oscillator strengths of electric-dipole transitions, are in quantitative agreement with the currently available experimental data in the low-stress region (<0.35 kbar).
3. For the case of high stress (up to 10 kbar), we provide a justification for the applicability of the theoretical model in the present calculation.
4. We explain the stress dependence of the acceptor levels, chemical shifts, and the oscillator strengths of the electric-dipole transition in terms of the compositions of the acceptor states.
5. We find some specific features in the high-stress region such as extra degeneracy of acceptor states and additional selection rules of the electric-dipole transitions. These features are also discussed in detail in the present dissertation.
6. We propose a scheme of high-efficiency THz radiation from a PQW laser incorporated with two different cavities. In this scheme, the two cavities can be simultaneously resonantly coupled with the PQWs. In this case, the device can emit EM waves of two different photon energies. One photon energy is the conduction-to-valence band energy gap, which is in the near-infrared (NIR) region; the other is the separation between the neighboring subbands. It is in the THz region.

7. We construct a theoretical model to analyze the system of PQWs incorporated with two different cavities. In this model, we take into account the heat generation caused by the acoustic deformation potential (ADP) scattering and the piezoelectric (PZ) scattering.
8. The calculation demonstrate that the THz surface emission power of 10 W/cm^2 can easily be achieved and the heat generation can be significantly suppressed and is almost constant with increasing current injection for high-power THz emission.

1.4 Organization

The dissertation is divided into two parts. The first part, from chapter 2 to chapter 4, is devoted to the study of group-III acceptors in strained Ge. In chapter 2, we review the earlier research of acceptor states and provide an overview of this part. In chapter 3, we present the theoretical model for the calculations of acceptor states and the oscillator strengths of electric-dipole transitions between the acceptor states. In chapter 4, we systematically present and discuss results for zero, infinitesimal, low, and high stress. The second part, including chapter 5 and chapter 6, is devoted to the study of parabolic quantum well laser with heterogeneous cavities. In chapter 5, we describe the operation principle of the devices and construct the theoretical model. In chapter 6, we present and discuss the results of the calculation for two different cases. In the first case, only a single cavity sustaining THz modes is present. In the second case, not only the THz cavity but also the cavity sustaining the NIR modes is present.

Part I.

Analysis of Group-III Acceptors in Ge under Uniaxial Stress

Chapter 2

Introduction

The electronic structures of impurities in semiconductor has been studied extensively experimentally [10] and theoretically [11] in the 1960s and 1970s. For the case of shallow impurities, the frequencies of the most prominent transitions are in general in the terahertz (THz) region [12-15]. Recently, research on shallow impurities in semiconductors has attracted considerable interest because they indicate that the shallow impurities are promising candidates for a simple and coherent THz radiation source [16]. It has been demonstrated that the THz radiation can be generated from group-III acceptors in Ge in the absence [17] and presence [9, 18-19] of stress. Therefore, it is important to study the stress effect on the electronic structures and on the oscillator strengths of the optical transitions between acceptor states for group-III acceptors in Ge.

In the theoretical aspect, it has been over half a century since the Luttinger-Kohn effective-mass approximation (EMA), which was first used to calculate the electronic structures of impurities in semiconductors [20]. However, the applicability of the EMA to the impurity problem is still an open issue, and modification within the framework of EMA is under development. Pantelides and Sah [21-22] evaluated the EMA by calculating the energy levels of donors in Si with *ab initio* impurity potentials. They found the EMA is not only applicable to shallow levels but also to deep levels for isocoric impurities, and the applicability can be extended to the case of nonisocoric impurities just by adding a reorthogonalization term to the impurity potential of [21]. Baldereschi and Lipari [23-24] calculated the energy levels of odd parity states for various group-III acceptors in Ge by EMA, giving results in quantitative agreement with experiments [12-15]. Their studies not only justify the applicability of the EMA to the group-III acceptors but also demonstrate the importance of the *q*-dependent di-

electric screening and the components of high angular momenta (up to l=7) of the acceptor states. The calculations of [23-24] show that the energy levels of odd parity states are almost independent of the species of the group-III acceptors. This is reasonable because the impurity potential difference between the group-III acceptors is significant only in the region around the impurity site (i.e., in the central-cell region), where the wave functions of the odd parity states are almost vanished. However, this is not so for even parity states. Lipari *et al.* [25] calculated the even parity states of various species of group-III acceptors by introducing into a semi-empirical impurity potential a short range part of a simple and local form. In addition, Buczko and Bassani [26] performed a similar calculation by using different impurity potential of a different form. The results of both [25] and [26] are in quantitative agreement with experiments. This provides the foundation for using the semi-empirical potential with the central-cell effect in the impurity level calculation.

The experimental absorption spectra of group-III acceptors in Ge have been available in [12-15] in 1960s and 1970s. Nevertheless, the quantitative values of oscillator strengths were not obtained until Rotsaert *et al* [27-28], in which the oscillator strengths is obtained by integrating the experimental absorption spectra. Clauws [29] *et al* calculated the oscillator strengths of electric-dipole transitions between ground states and odd-parity states in EMA. Their calculation also introduces into a semi-empirical impurity potential a short range part of a simple and local form, which is different from that of Buczko and Bassani [26]. The results of [29] and [26] are in quantitative agreement. However they are not in quantitative agreement with the experimental results of [27-28]. Furthermore, Andreev *et al* [30-31] determined not only the oscillator strengths but also the linewidth by very-high resolution (up to 0.01 cm^{-1}) absorption spectra. The experimental results of oscillator strengths are in quantitative agreement with the theoretical data [26, 29], but not with the experiments [27-28]. Andreev *et al* [31] proposed that the possible reason of the disagreement between experimental results of

Rotsaert *et al* [27-28] and Andreev *et al* [30-31] is the difference in resolutions of the spectra.

Several studies have been done regarding the stress effect on the acceptor levels [32-34] and on the on the oscillator strengths of the electric-dipole transitions [35]. However, none of them considers simultaneously the *q*-dependent dielectric screening and the central-cell correction. In addition, the axial approximation have been used in [35]. It is not reasonable at low stress.

In part I of the dissertation, we study the stress effect on the electronic structure and the oscillator strength of electric-dipole transitions for various group-III acceptors in Ge by the EMA with a simple semi-empirical potential including the *q*-dependent dielectric screening and the central-cell correction. The details of the calculation method are presented in chapter 2, and the results and discussion in chapter 3. In section 3.1, we make assignments of the experimental transition lines in the absence of stress. We also discuss the correlation between the central-cell potential and the oscillator strength of electric-dipole transitions. In section 3.2, we discuss the effect of an infinitesimal stress on the oscillator strengths, and calculate the intensity parameters *u* and *v*, which are parameters to determine the relative intensities of the infinitesimal-stress-induced components of the electric-dipole transitions between Γ_8 acceptor states for the zincblend structure host crystal. In section 3.3, we discuss in detail the stress dependence of the oscillator strength of the electric-dipole transitions and the low-lying acceptor levels in the low-stress region (<0.35 kbar). In addition, we make assignments for the currently available experimental lines of stress-induced components. In section 3.4, we study the general stress effect on the acceptor electronic structure. To do this, the stress in the section is up to 10 kbar. The tensile stress is also considered for convenience in comparison and analysis. In section 3.5, we discuss some specific features in the high stress region in which the coupling between the heavy-hole (HH) and the light-hole (LH) is negligible. Finally, we give a justification of the impurity potential adopted in the present calculation.

Chapter 3

Calculation Method

3.1 Electronic Structure

We calculate the electronic structure of the acceptor states in strained group-III germanium by means of the six-band Lutteinger-Kohn effective mass Hamiltonian [20] modified by the Bir-Pikus deformation theory [36]. In this scheme, the acceptor states can be expressed as

$$\left|\Psi\right\rangle = \sum_{j=1}^{6} F_j \left| J^j M^j \right\rangle, \tag{3.1}$$

where |3/2,±3/2>, |3/2,±1/2> , and |1/2,±1/2> are the HH, LH, and split-off-hole (SO) band edge states, respectively. The $|J^j,M^j>$ transform in the $T_d^{'}$ group like the spherical harmonic function $Y_{J^j M^j}$. The |3/2,±3/2> and |3/2,±1/2> are basis functions of the Γ_8 representation; the |1/2,±1/2> are basis functions of Γ_7 representation. The F_j are the envelope functions which are the solutions of the effective-mass equation,

$$\sum_{j=1}^{6} H_{ij} F_j = E F_j, \qquad j = 1, 2, ..., 6, \tag{3.2}$$

where E is the energy of the acceptor states and H_{ij} the elements of the effective-mass Hamiltonian H. The H can be expressed as a sum of the Hamiltonian without acceptors H_0 (i.e., the Hamiltonian of the perfect crystal) and the remaining part caused by the presence of the acceptors,

$$VI = H - H_0, \tag{3.3}$$

where V is the impurity potential, I is a 6×6 unit matrix. The general form of H_0 can be expressed as [34, 37]

$$H_0 = \begin{bmatrix} P+Q & -S & R & 0 & -\frac{1}{\sqrt{2}}S & \sqrt{2}R \\ -S^{\dagger} & P-Q & 0 & R & -\sqrt{2}Q & \sqrt{\frac{3}{2}}S \\ R^{\dagger\dagger} & 0 & P-Q & S & \sqrt{\frac{3}{2}}S & \sqrt{2}Q \\ 0 & R^{\dagger\dagger\dagger\dagger} & S & P+Q & -\sqrt{2}R & -\frac{1}{\sqrt{2}}S \\ -\frac{1}{\sqrt{2}}S^{\dagger} & -\sqrt{2}Q & \sqrt{\frac{3}{2}}S & -\sqrt{2}R & P+\Delta & 0 \\ \sqrt{2}R^{\dagger\dagger} & \sqrt{\frac{3}{2}}S & \sqrt{2}Q & -\frac{1}{\sqrt{2}}S & 0 & P+\Delta \end{bmatrix} \begin{matrix} \left|\frac{3}{2},\frac{3}{2}\right\rangle \\ \left|\frac{3}{2},\frac{1}{2}\right\rangle \\ \left|\frac{3}{2},-\frac{1}{2}\right\rangle \\ \left|\frac{3}{2},-\frac{3}{2}\right\rangle \\ \left|\frac{1}{2},\frac{1}{2}\right\rangle \\ \left|\frac{1}{2},-\frac{1}{2}\right\rangle \end{matrix}, \tag{3.4}$$

where

$$P = P_k + P_\varepsilon, \quad Q = Q_k + Q_\varepsilon$$
$$R = R_k + R_\varepsilon, \quad S = S_k + S_\varepsilon$$
$$P_k = \left(\frac{\gamma_1}{2m_0}\right)\left(p_x^2 + p_y^2 + p_z^2\right)$$
$$Q_k = \left(\frac{\gamma_2}{2m_0}\right)\left(p_x^2 + p_y^2 - 2p_z^2\right)$$
$$R_k = \left(\frac{\sqrt{3}}{2m_0}\right)\left[-\gamma_2\left(p_x^2 - p_y^2\right) + 2i\gamma_3 p_x p_y\right]$$
$$S_k = \left(\frac{\sqrt{3}\gamma_3}{m_0}\right)\left(p_x - ip_y\right)p_z$$

$$P_\varepsilon = -a_v\left(\varepsilon_{xx} + \varepsilon_{yy} + \varepsilon_{zz}\right), \; Q_\varepsilon = -\frac{b}{2}\left(\varepsilon_{xx} + \varepsilon_{yy} - 2\varepsilon_{zz}\right)$$
$$R_\varepsilon = \frac{\sqrt{3}}{2}b\left(\varepsilon_{xx} - \varepsilon_{yy}\right) - id\varepsilon_{xy}, \; S_\varepsilon = -d\left(\varepsilon_{xz} - i\varepsilon_{yz}\right)$$

.

The $p_x = -i\hbar\partial/\partial x$, $p_y = -i\hbar\partial/\partial y$, and $p_z = -i\hbar\partial/\partial z$ are the elements momentum operator along the crystallographic directions [100], [010], and [001], respectively; ε_{ij} is the symmetric strain tensor; Δ is the spin-orbit split-off energy, γ_1, γ_2, and γ_3 are the Luttinger parameters; a_v, b, and d are the Pikus-Bir deformation potentials; m_0 is the free-electron mass. For the case of a stress P along the [001] direction, only the normal strains ε_{xx}, ε_{yy}, and ε_{zz} are not vanished.

They can be written as

$$\begin{aligned} \varepsilon_{xx} &= \varepsilon_{yy} = \frac{C_{12}}{2C_{12}^2 - C_{11}C_{12} - C_{11}^2} P \\ \varepsilon_{zz} &= -\frac{C_{11} + C_{12}}{2C_{12}^2 - C_{11}C_{12} - C_{11}^2} P \end{aligned}, \tag{3.5}$$

where C_{11} and C_{12} are stiffness constants. Because the strain ε_{xx} is equal to ε_{yy}, R_ε=S_ε=0. Therefore, we need only the deformation potential b in the calculation if we neglect the P_ε wich just shifts the valence bands as a whole. The impurity potential is a sum of the Coulomb contribution V_C and the central-cell correction V_{cc} and is expressed in a semi-empirical form:

$$\begin{aligned} V &= V_C + V_{cc} \\ V_C &= -\frac{q^2}{\epsilon r}\left[1 + (\epsilon - 1)\exp\left(-\frac{\alpha r}{a_B^*}\right)\right], \\ V_{cc} &= \frac{Aq^2}{2\epsilon r}\exp\left(-\frac{\beta r}{a_B^*}\right) \end{aligned} \tag{3.6}$$

where α, β, and A are dimensionless parameters; ϵ is the dielectric constant; q is the elementary charge; $a_B^* = \epsilon\gamma_1\hbar^2 / m_0 e^2$ is the effective Bohr radius. The Coulomb contribution V_C is caused by the point charge of the acceptor ion modified by the q-dependent dielectric screening [25]. The V_{cc} includes the contributions (a) the difference in the screened potential induced by the positive point charge at the impurity site with the charge magnitude equal to that of the core electrons between the impurity and the host atoms, (b) the difference in the screened potentials induced by the core electrons between the impurity and the host atoms, (c) the difference in the effective repulsive potentials, which is the kinetic energy of the valence electrons in nature, localized in the central-cell region, and originates from the requirement that the wave functions of the valence electrons are orthogonal to those of the core electrons, (d) the lattice relaxation around the impurity site induced by the presence of the impurity [21-22]. The sum of the contribution (a) and the V_C is just the difference in the screened point charge potential induced by the nucleus. The sum of the potentials (a) and (b) is attractive for

the valence electrons and localized in the central-cell region because they are induced by charges of the same magnitude but opposite sign. The effect (c) should be the primary contribution. Therefore, we expect that the V_{cc} is small for the isocoric acceptor Ga, positive (A>0) for B and Al, and negative (A<0) for In and Tl.

In order to solve the effective-mass equation (3.2), the envelope function can be expanded in a sum of products of radial functions and spherical harmonic functions,

$$F_j = \sum_{lm} g_{jlm}(r) Y_{lm}(\theta,\phi). \tag{3.7}$$

To save the labor in the calculation, we take into account the symmetry of the acceptor states. In the absence of stress, the acceptor states transform like basis functions of the irreducible representations Γ_6, Γ_7, and Γ_8 of the T_d' group. In the presence of stress along the [001] direction, the Γ_8 state of the T_d' group split into one Γ_6 and one Γ_7 states of the D_{2d}' group, and the $\Gamma_6(\Gamma_7)$ state of the T_d' group becomes the $\Gamma_6(\Gamma_7)$ state of the D_{2d}' group. Both the Γ_6 and the Γ_7 states are doubly degenerate because of the time reversal symmetry. Furthermore, in spite of the lack of the inversion symmetry of the problem, all the envelope functions of an acceptor states have a common parity because the effective-mass Hamiltonian H has inversion symmetry about the impurity site. Therefore, the acceptor state can be classified to Γ_6^+, Γ_6^-, Γ_7^+ ,and Γ_7^- states, where the even- (odd-) parity of the envelope function is denoted by the superscript + (–). For the even- (odd-) parity states, the sum in Eq. (3.7) over l runs over all nonnegative even (odd) integers; the sum over m runs over the integers

$$m=\begin{cases} 4n+\dfrac{3}{2}-M^{j} & \text{for } \Gamma_6^+ \\ 4n+\dfrac{1}{2}-M^{j} & \text{for } \Gamma_7^+ \\ 4n-\dfrac{1}{2}-M^{j} & \text{for } \Gamma_6^- \\ 4n-\dfrac{3}{2}-M^{j} & \text{for } \Gamma_7^- \end{cases}, \tag{3.8}$$

where n is an integer. Such a choice of the basis functions of the angular part of the envelope functions is equivalent to that in Ref. [34] although different in formulation. The radial part of the envelope function is expanded as

$$g_{jlm}(r)=r^{L}\sum_{\nu}c_{j\nu}^{lm}e^{-\alpha_{\nu}r}, \tag{3.9}$$

where the numbers α_ν are chosen to form a geometric progression [26]. The value L is chosen according to the following rule

$$L=\begin{cases} 0 & \text{for } l=0 \\ 1 & \text{for } l=1 \text{ and any positive even number} \\ 2 & \text{for } l=\text{any odd number except for 1} \end{cases} \tag{3.10}$$

3.2 Electric-Dipole Transitions

Having obtained the acceptor states, we can go on to calculate the electric-dipole transitions between these states. Considering the case that the temperature T=4.22 K, we suppose that all the holes are in the ground state $1\Gamma_8^+$ in the absence of stress, and in the $1\Gamma_6^+$ and the $1\Gamma_7^+$ states, into which the $1\Gamma_8^+$ splits when a [001] stress is applied. Thus, the absorption coefficient of the electric-dipole transition between acceptor states can be written as

$$\alpha(\hbar\omega;\mathbf{e})=\frac{2\pi^{2}\hbar q^{2}\gamma_{1}N_{a}}{cm_{0}\sqrt{\epsilon}}\sum_{\mu\nu}\sum_{n=1}^{\infty}w\left(1\Gamma_{\mu}^{+}\right)f_{1\Gamma_{\mu}^{+},n\Gamma_{\nu}^{-}}(\mathbf{e})\,\delta\left(E\left(n\Gamma_{\nu}^{-}\right)-E\left(1\Gamma_{\mu}^{+}\right)+\hbar\omega\right), \tag{3.11}$$

where $n\Gamma_\nu^u$ (u=+,–) denotes the nth lowest Γ_ν^u acceptor state, $E\left(n\Gamma_\nu^u\right)$ is the energy level of the $n\Gamma_\nu^u$ state, **e** is the polarization unit vector of the EM wave, $w\left(1\Gamma_\mu^+\right)$ is the probability that a hole is in the $1\Gamma_\mu^+$ state, N_a is the acceptor concentration. The indices μ and ν run over all the irreducible representation. The $f_{1\Gamma_\mu^+,n\Gamma_\nu^-}(\mathbf{e})$ is the oscillator strength of the electric-dipole transition from the $1\Gamma_\mu^+$ state to the $n\Gamma_\nu^-$ state [38],

$$f_{1\Gamma_\mu^+,n\Gamma_\nu^-}(\mathbf{e})=\frac{2m_0}{\gamma_1\hbar^2}\frac{1}{g_\mu}\left(E\left(n\Gamma_\nu^-\right)-E\left(1\Gamma_\mu^+\right)\right)\sum_{qq'}\left|\left\langle 1\Gamma_{\mu(q)}^+\left|\mathbf{e}\bullet\mathbf{r}\right|n\Gamma_{\nu(q')}^-\right\rangle\right|^2, \tag{3.12}$$

where g_μ is the degeneracy of the $1\Gamma_\mu^+$ state, and the q (q') runs over all the degenerate partners of the $1\Gamma_\mu^+$ ($n\Gamma_\nu^-$) state. There are four terms in the sum of Eq. (3.12) for the case of the $D_{2d}^{'}$ group. Two of them are zero if we choose an appropriate orthogonal set of the degenerate states. The remaining two terms have the same value because of the time reversal symmetry. Therefore, Eq. (3.12) can be expressed as

$$f_{1\Gamma_\mu^+,n\Gamma_\nu^-}(\mathbf{e})=\frac{4m_0}{\gamma_1\hbar^2}\left(E\left(n\Gamma_\nu^-\right)-E\left(1\Gamma_\mu^+\right)\right)\left|\left\langle 1\Gamma_\mu^+\left|\mathbf{e}\bullet\mathbf{r}\right|n\Gamma_\nu^-\right\rangle\right|^2. \tag{3.13}$$

Here, for simplicity, we drop the indices q and q', and the $\left\langle 1\Gamma_\mu^+\left|\mathbf{e}\bullet\mathbf{r}\right|n\Gamma_\nu^-\right\rangle$ is one of the non-zero matrix elements. By Eqs. (3.1) and (3.7), the matrix element $\left\langle 1\Gamma_\mu^+\left|\mathbf{e}\bullet\mathbf{r}\right|n\Gamma_\nu^-\right\rangle$ can be further expressed as

$$\left\langle 1\Gamma_\mu^+\left|\mathbf{e}\bullet\mathbf{r}\right|n\Gamma_\nu^-\right\rangle=\sum_{l}^{(\text{even})}\sum_{\substack{l'=l\pm1\\ l'\geq1}}\sum_{mm'}\sum_{j=1}^{6}\int_0^\infty drr^3 g_{jlm}^{1\Gamma_\mu^+*}g_{j'l'm'}^{n\Gamma_\nu^-}\int_0^{2\pi}d\phi\int_{\theta=0}^{\pi}\sin\theta d\theta Y_{lm}^*Y_{l'm'}\cos\theta_r \tag{3.14}$$

where θ_r is the angle between **e** and **r**. Here, the envelope functions have been supposed to be slowly varying compared with the Bloch functions because they are really slowly varying outside the central-cell region. Inside the central-cell region, the wavefunctions of odd-parity states are almost vanished so that treating the envelope functions as slowly varying functions

will not considerably affect the result of the integration (3.14).

In the present calculation, we denote the EM wave with the polarization vector parallel (perpendicular) to the stress direction [001] by $\mathbf{E}_{\|}$ ($\mathbf{E}_{\perp}$). For $\mathbf{E}_{\|}$, the $1\Gamma_6^+ \to n\Gamma_6^-$ and $1\Gamma_7^+ \to n\Gamma_7^-$ the transitions are forbidden, while for $\mathbf{E}_{\perp}$, all the transitions are allowed.

3.3 Values of Parameters

In the present calculation, the parameters of bulk Ge are set as follows: the Luttinger's parameters γ_1=13.38, γ_2=4.24 and γ_3=5.69 [39], the spin-orbit splitting Δ=296 meV [40], the stiffness constants C_{11}=1240 kbar/cm^2 and C_{12}=413 kbar/cm^2 [41], and the deformation potential b=-2.63 eV. The value of the deformation potential is determined by a best fit to the experimental stress dependence of the transition energy between $1\Gamma_6^+$ and $1\Gamma_7^+$ [42]. The dielectric constant ϵ and the parameter α for the acceptor Coulomb potential are set at 15.36 and 0.93 $\epsilon\gamma_1$, respectively, as in the work of [25] and [43]. For the central-cell potential, β is set at 1.00 $\epsilon\gamma_1$ and A is an adjustable parameter, as in the work of [44]. By fitting the calculated to the experimental values of the D line transition energy (i.e., the energy difference between $1\Gamma_8^+$ and $2\Gamma_8^-$) for various species of acceptors in Ge [12-14], we determine the A values to be 28.96, 7.52, 1.00, –13.71 and –26.29 for B, Al, Ga, In and Tl, respectively. This is in agreement with our expectation in section 2.1 that the V_{cc} (and hence the value of parameter A) is is small for the isocoric acceptor Ga, positive (A>0) for B and Al, and negative (A<0) for In and Tl.

Chapter 4

Results and Discussion

4.1 **Zero Stress**

We make assignments for the lines associated with transitions from the ground state $1\Gamma_8^+$ to the odd-parity states. Table 4.1 lists the calculated transition energies, together with experimental data currently accessible, for various species of acceptors in unstrained Ge. As can be seen, our calculation not only results in excellent assignments but also resolves crowding levels of final states for observed single transitions which have not been resolved by experiment. For instance, the A_3 line is associated with the transitions $1\Gamma_8^+ \to \left(2\Gamma_7^-, 1\Gamma_6^-, 6\Gamma_8^-\right)$.

Table 4.2 lists the calculated transition energies for the hole from the lowest odd-parity state $1\Gamma_8^-$ to the higher even-parity states of unstrained Ge:B together with the experimental data of [45]. Lipari *et al*. [25] and Kurskii [46] have identified a single level of $2\Gamma_8^+$ for Ge:B by assigning the *E* line in [12] to the transition from $1\Gamma_8^+$ to $2\Gamma_8^+$. Here, we identify systematically the levels of even-parity states by assigning the lines of transitions in [45]. The assignment is found to be excellent. Furthermore, our calculation can give additional energy levels of even-parity states which have not been resolved yet by experiment. In [45], the lines of 2.435 and 2.485 meV are associated with $G^* \to C^*$ transition where the symbol G^* corresponds to the $1\Gamma_8^-$ level and the C^* corresponds to the set of the $3\Gamma_8^+$, $1\Gamma_7^-$, and $3\Gamma_8^-$ levels. Excluding the $1\Gamma_8^- \to 1\Gamma_7^-$, and $1\Gamma_8^- \to 3\Gamma_8^-$ transitions which are almost electric-dipole forbidden, we assign the line at 2.435 meV to the $1\Gamma_8^- \to 3\Gamma_8^+$ transition while the line at 2.485 meV is assigned to the $2\Gamma_8^+ \to 3\Gamma_6^-$ transition whose energy is 2.481 meV in our calculation.

Figure 4.1 shows the oscillator strengths as functions of the parameter A for electric-dipole transitions of $G(1\Gamma_8^+ \rightarrow 1\Gamma_8^-)$, $D(1\Gamma_8^+ \rightarrow 2\Gamma_8^-)$, and $C(1\Gamma_8^+ \rightarrow 1\Gamma_7^-, 3\Gamma_8^-)$ lines. The parameter A can be regarded as the strength of the effective central-cell force exerted on the hole. It is positive (negative) for the effective repulsive (attractive) force for the hole. As can be seen, the oscillator strengths decrease with the attractive force. This is because the probability of the hole in the central-cell region increases with the attractive force for the ground state and the integral in Eq. (3.14) over the central-cell region gives almost no contribution to the whole dipole matrix element. The oscillator strengths almost vanish when the attractive force is so large that the wave function of the ground state is totally localized in the central-cell region (A<50). On the other hand, the oscillator strengths increase slowly with the repulsive force because the size of central-cell region is much smaller than that of the ground-state wave function. As a result, the deviation of the oscillator strength of the D line transition from that of the pure point charge (with A=0) for Tl is three times larger in magnitude than that for B, even though the magnitude of A for Tl is smaller than that for B. The dashed line in Fig. 4.1 is for the binding energy of the ground state. It decreases slowly with the repulsive force, but increases dramatically with the attractive force when the attractive force is so large (A<–35) that an appreciable part of the wave function of the ground state is localized in the central-cell region. When this happens, the effective mass theory is no longer applicable. The points in Fig. 4.1 are the oscillator strengths measured by Andreev *et al.* [30-31] for acceptors B and Al. As can be seen, there is an excellent agreement between the calculated and the experimental results.

Table 4.1 Transition energies from the ground state $1\Gamma_8^+$ to the odd-parity states for various group-III acceptors in unstrained Ge. The symbols for transition lines given in the first column are defined as in [14].

		Transition energy from $1\Gamma_8^+$ (meV)									
Line	Final state	B		Al		Ga		In		Tl	
G	$1\Gamma_8^-$	6.233[a]	6.21[b]	6.569[a]	6.59[c]	6.734[a]	6.72[d]	7.376[a]		8.848[a]	8.91[b]
		6.24[c]	6.215[d]	6.565[d]	6.581[e]	6.74[c]		7.39[c]		8.87[c]	
D	$2\Gamma_8^-$	7.936[a]	7.936[b]	8.272[a]	8.27[c]	8.437[a]	8.437[d]	9.080[a]	9.113[d]	10.551[a]	10.552[b]
		7.94[c]	7.936[d]	8.272[d]	8.28[e]	8.44[c]	8.441[e]	9.08[c]		10.57[c]	
C	$1\Gamma_7^-$	8.685[a]	8.681[b]	9.021[a]	9.02[c]	9.186[a]	9.185[d]	9.829[a]	9.864[d]	11.301[a]	11.3[b]
		8.69[c]	8.686[d]	9.025[d]	9.031[e]	9.19[c]	9.192[e]	9.86[c]		11.32[c]	
	$3\Gamma_8^-$	8.707[a]		9.043[a]		9.208[a]		9.851[a]		11.322[a]	
B	$4\Gamma_8^-$	9.329[a]	9.33[b]	9.666[a]	9.67[c]	9.831[a]	9.814[d]	10.473[a]	10.506[d]	11.945[a]	11.93[b]
		9.32[c]	9.32[d]	9.654[d]	9.665[e]	9.84[c]	9.825[e]	10.48[c]		11.92[c]	
A_4	$5\Gamma_8^-$	9.593[a]		9.929[a]	9.925[e]	10.094[a]		10.736[a]		12.208[a]	
		9.568[d]		9.927[d]		10.091[d]		10.746[d]			
A_3	$2\Gamma_7^-$	9.665[a]	9.66[b]	10.002[a]	10.02[c]	10.167[a]	10.152[d]	10.809[a]	10.828[d]	12.281[a]	12.29[b]
		9.65[c]	9.665[d]	9.995[d]	10.001[e]	10.17[c]		10.81[c]		12.26[c]	
	$1\Gamma_6^-$	9.669[a]		10.005[a]		10.170[a]		10.813[a]		12.285[a]	
	$6\Gamma_8^-$	9.682[a]		10.018[a]		10.183[a]		10.826[a]		12.297[a]	
A_2	$3\Gamma_7^-$	9.798[a]	9.79[b]	10.134[a]	10.15[c]	10.299[a]	10.287[d]	10.942[a]	10.955[d]	12.413[a]	12.42[b]
		9.81[c]	9.785[d]	10.13[d]	10.113[e]	10.31[c]		10.96[c]		12.43[c]	
A_1	$7\Gamma_8^-$	9.879[a]	9.863[d]	10.215[a]	10.198[d]	10.380[a]	10.36[d]	11.023[a]	11.033[d]	12.494[a]	

[a] present work; [b] reference [13]; [c] reference[12]; [d] reference [14]; [e] reference [15].

Table 4.2 The transition energies from the $1\Gamma_8^-$ state to the higher even-parity states of unstrained Ge:B. The experimental data are taken from [45], and the number in parentheses attached to each of the data is the sample number.

	Transition energy from $1\Gamma_8^-$ (meV)	
Final state	Present work	Experimental data
$2\Gamma_8^+$	1.36	1.365 (23)
$3\Gamma_8^+$	2.43	2.435 (44)
$1\Gamma_6^+$	2.85	2.865 (48)
$4\Gamma_8^+$	2.92	2.91 (49)
$1\Gamma_7^+$	3.25	3.26 (51)
$5\Gamma_8^+$	3.30	3.3 (52)
$6\Gamma_8^+$	3.36	3.37 (53)
$2\Gamma_6^+$	3.47	3.48 (54)
$7\Gamma_8^+$	3.55	
$3\Gamma_6^+$	3.58	3.585 (55)
$2\Gamma_7^+$	3.75	
$8\Gamma_8^+$	3.76	
$9\Gamma_8^+$	3.79	3.79 (56)
$10\Gamma_8^+$	3.84	
$4\Gamma_6^+$	3.87	
$11\Gamma_8^+$	3.88	3.875 (57)
$3\Gamma_7^+$	3.88	
$12\Gamma_8^+$	3.90	3.89 (58)
$5\Gamma_6^+$	3.92	3.925 (59)

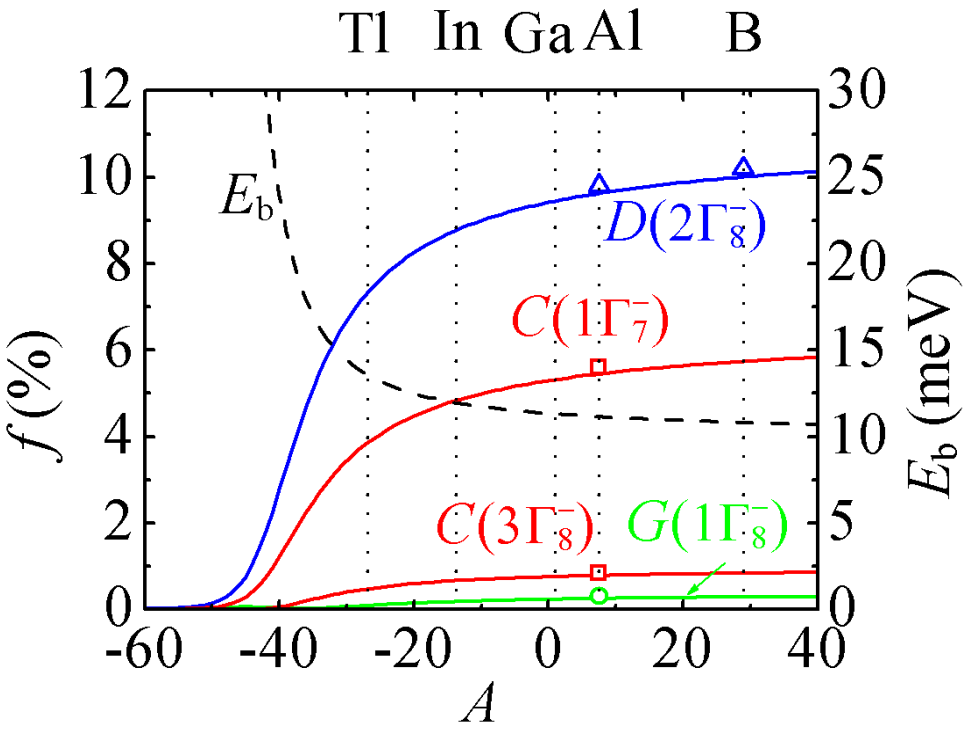

Fig. 4.1 Oscillator strengths of electric-dipole transitions for $G(1\Gamma_8^+ \to 1\Gamma_8^-)$, $D(1\Gamma_8^+ \to 2\Gamma_8^-)$, and $C(1\Gamma_8^+ \to 1\Gamma_7^-, 3\Gamma_8^-)$ lines and the binding energy of the ground state as functions of the strength parameter *A*. The points are experimental data of [30-31].

4.2 **Infinitesimal Stress**

As mentioned earlier, the uniaxial stress along the [001] direction will reduce the crystal symmetry from T_d group to D_{2d} group. In order to avoid confusing the notations of $T_d^{'}$ group and $D_{2d}^{'}$ group, we denote the irreducible representations, symmetry, and acceptor states of $T_d^{'}$ group by $\overline{\Gamma}_\nu$, $\overline{\Gamma}_\nu^u$, and $n\overline{\Gamma}_\nu^u$ (i.e., the symbols with a bar), respectively, in the following discussion.

The relative intensities of the infinitesimal-stress-induced components of the $\overline{\Gamma}_8 \to \overline{\Gamma}_6$ and the $\overline{\Gamma}_8 \to \overline{\Gamma}_7$ transitions can be determined by the group-theoretical analysis, and those of the $\overline{\Gamma}_8 \to \overline{\Gamma}_8$ transitions depend on two intensity parameters u and v [47]. For $\mathbf{E}_{\|}$, the relative intensities of the $\Gamma_6 \to \Gamma_7$ and the $\Gamma_7 \to \Gamma_6$ components are 1/2–v and 1/2+v, respectively. For $\mathbf{E}_{\perp}$, those of the $\Gamma_6 \to \Gamma_6$, the $\Gamma_6 \to \Gamma_7$, the $\Gamma_7 \to \Gamma_6$, and the $\Gamma_7 \to \Gamma_7$ components are 3u/8, (1–3u/4+v)/2, (1–3u/4–v)/2, and 3u/8, respectively. The values of u and v of the $1\overline{\Gamma}_8^+ \to n\overline{\Gamma}_8^-$ transitions for various species of group-III acceptors in Ge are listed in Table 4.3. As can be seen, the intensity parameters (and hence the relative intensities) do not correlate significantly with the species of group-III acceptors except for the $1\overline{\Gamma}_8^+ \to 1\overline{\Gamma}_8^-$ transition. Martin *et al*. obtained the values of the parameters, u=0.95±0.05 and v=–0.1±0.05, for Ge:Ga by the piezospectroscopic measurement [48]. Our result, u=0.99 and v=–0.10, shows a better agreement with the experiment than that of [34], u=0.91 and v=–0.29.

Table 4.3 Intensity parameters for group-III acceptors in Ge.

	B		Al		Ga		In		Tl	
Final state	u	v	u	v	u	v	u	v	u	v
$1\Gamma_8^-$	0.98	−0.13	0.99	−0.11	0.99	−0.10	1.00	−0.07	1.00	0.04
$2\Gamma_8^-$	0.12	0.33	0.12	0.33	0.12	0.33	0.13	0.33	0.13	0.33
$3\Gamma_8^-$	0.79	−0.41	0.79	−0.41	0.79	−0.41	0.79	−0.41	0.79	−0.40
$4\Gamma_8^-$	0.08	0.27	0.08	0.28	0.09	0.28	0.09	0.29	0.10	0.30

4.3 Oscillator Strengths and Line Assignment in the Low-Stress Region

Even though the group-theoretical analysis of [47] provides information about the relative intensities at infinitesimal stress, it is not applicable to the case of finite stress due to the strain-induced couplings between acceptor states of the same symmetry. In this section, we consider the presence of a finite but low stress (≤0.3 kbar). In such a low-stress region, the energy levels of the initial and the final states of the *G*, *D*, and *C* line components do not either cross or anticross.

4.3.1 ***G-line***

In the presence of [001] stress, the *G* line splits into four components, $G_1(1\Gamma_6^+ \rightarrow 1\Gamma_6^-)$, $G_2(1\Gamma_6^+ \rightarrow 1\Gamma_7^-)$, $G_3(1\Gamma_7^+ \rightarrow 1\Gamma_6^-)$, and $G_4(1\Gamma_7^+ \rightarrow 1\Gamma_7^-)$. Figure 4.2 shows the stress dependence of the oscillator strengths of the *G* line components for (a) $\mathbf{E}_{\parallel}$ and (b) $\mathbf{E}_{\perp}$. As can be seen, the oscillator strengths are susceptible to the stress in the low-stress region. In addition, with the increase of stress, the oscillator strengths of G_1 for $\mathbf{E}_{\perp}$ and G_2 for $\mathbf{E}_{\parallel}$ first decrease to zero and then increase.

We further inspect the compositions of acceptor states to gain more insight into the stress dependence of oscillator strengths. In the absence of stress, the initial states of the *G* line components, $1\Gamma_6^+$ and $1\Gamma_7^+$, have an s (*l*=0) composition of 71% and a d (*l*=2) composition of 28%. The final states, $1\Gamma_6^-$ and $1\Gamma_7^-$, have a p (*l*=1) composition of 90% and an f (*l*=3) composition of 9%. In the stress region from 0 to 0.3 kbar, the compositions are not susceptible to the stress because the couplings of the $1\Gamma_6^+$, $1\Gamma_7^+$, $1\Gamma_6^-$, and $1\Gamma_7^-$ states with other acceptor

states of the same symmetry are weak. As a result, the dipole matrix elements of Eq. (3.14) contain significant s→p and d→p components (denoted by M_{sp} and M_{dp}, respectively), a small d→f component M_{df}, and negligible higher-order components. Furthermore, the components M_{sp} and M_{dp} have comparable magnitudes but opposite signs so that the sum of M_{sp} and M_{dp} is small in magnitude and comparable with M_{df}. This is the reason why the oscillator strength of the *G* line transition, as Fig. 4.1 shows, is much smaller than those of the *C* and *D* line transitions, even though the final state of the *G* line transition has a greater overlap with the ground state than those of *C* and *D* line transitions. Because of the significant overlap between the wave functions of the initial and the final states, and the almost complete cancellation between the M_{sp} and the M_{dp} components, the weak strain-induced couplings between the acceptor states still has a considerable influence on the stress dependence of oscillator strengths as Fig. 4.2 shows.

As to the G_1 line for $\mathbf{E}_\perp$ and the G_2 linefor $\mathbf{E}_\parallel$, M_{sp} has a larger magnitude than M_{dp} and has the same sign as M_{df} at zero stress. With the increase of stress, M_{sp} (M_{dp}) decreases (increases) markedly in magnitude, but M_{df} changes slowly. Therefore, the oscillator strength decreases with stress until it reduces to zero. If the stress goes on increasing, the M_{dp} becomes larger in magnitude than the sum of M_{sp} and M_{df}, leading to the increase in the oscillator strength with stress.

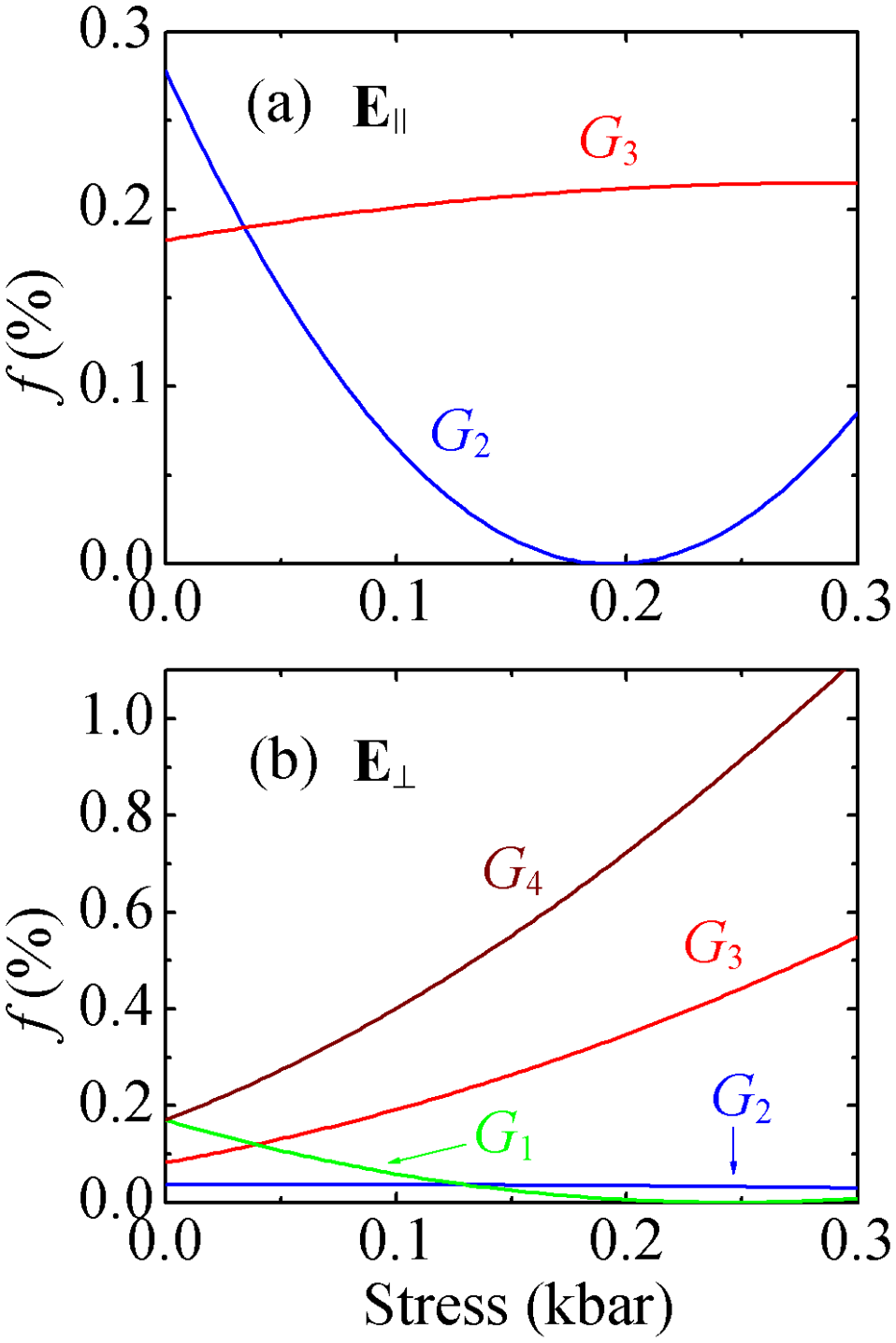

Fig. 4.2 Oscillator strengths of *G* line components for Ge:Ga as functions of uniaxial stress along the [001] direction for (a) $\mathbf{E}_{\parallel}$ and (b) $\mathbf{E}_{\perp}$.

4.3.2 ***D-line***

The final state of *D* line transition has a 55% p and a 43% f compositions at zero stress. The sum of M_{sp}, M_{dp}, and M_{df}, unlike the G line transition, is not small in magnitude. Therefore, the *D* line transition is one of the most prominent transitions as Fig. 4.1 shows.

In the presence of [001] stress, the *D* line splits into four components, $D_1(1\Gamma_6^+ \rightarrow 2\Gamma_6^-)$, $D_2(1\Gamma_6^+ \rightarrow 2\Gamma_7^-)$, $D_3(1\Gamma_7^+ \rightarrow 2\Gamma_6^-)$, and $D_4(1\Gamma_7^+ \rightarrow 2\Gamma_7^-)$. Figure 4.3 shows the assigned transition energies of the *D* line components as well as *C* and *B* line components for Ge:In against the [001] stress, together with the experimental data of [49] for comparison. As can be seen, the calculated results show excellent agreement with the experimental results. This confirms the reliability of our calculation in the low-stress region. The D_1 and the D_4 transitions are not observed in [49]. They are more difficult to be observed than the D_2 and the D_3 transitions. This can be seen in Fig. 4.4, in which the D_1 and the D_4 transitions are forbidden for $\mathbf{E}_{\parallel}$ and their oscillator strengths are much smaller than those of the D_2 and the D_3 transitions for $\mathbf{E}_{\perp}$.

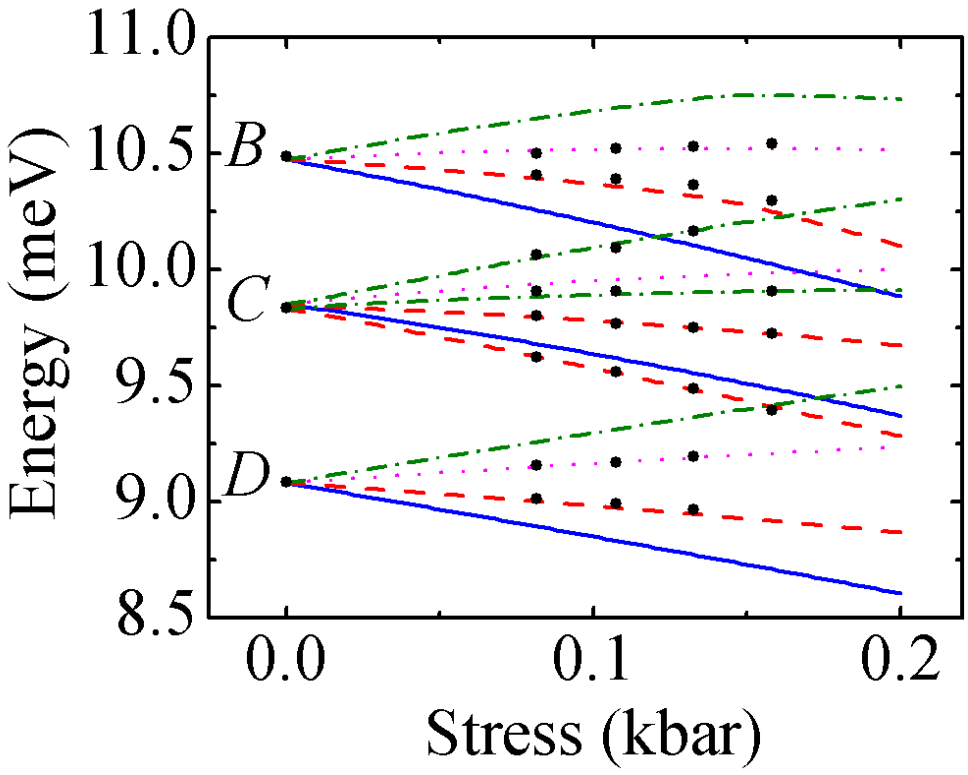

Fig. 4.3 Stress dependence of transition energies of the *B*, the *C*, and the *D* lines for Ge:In. The solid circles represent the experimental data taken from [49]. The lines are for the calculated transition energies from the $1\Gamma_6^+$ to the Γ_6^- states (solid lines), from the $1\Gamma_6^+$ to the Γ_7^- states (dashed lines), from the $1\Gamma_7^+$ to the Γ_6^- states (dotted lines), and from the $1\Gamma_7^+$ to the Γ_7^- states (dash-dotted lines).

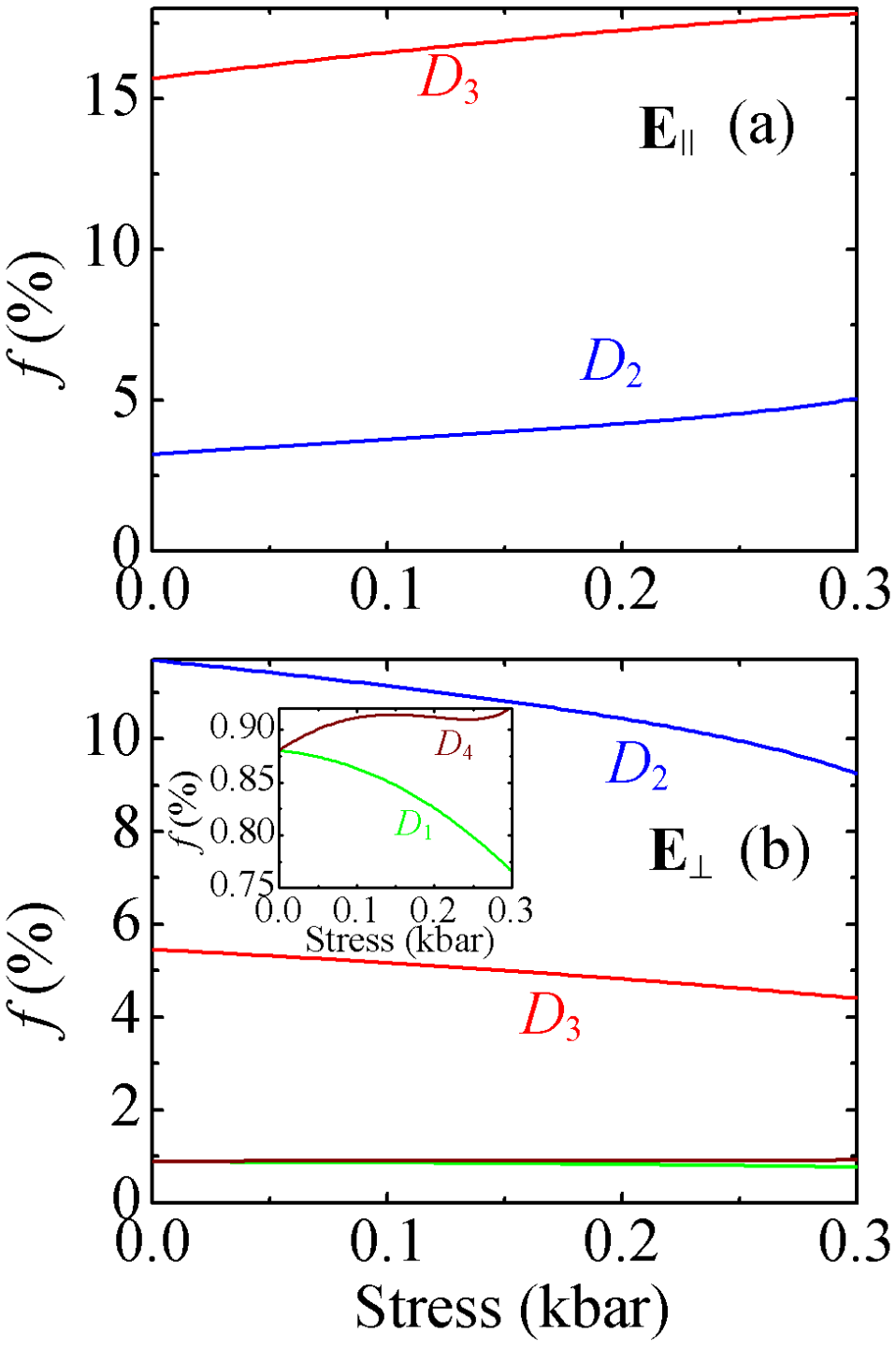

Fig. 4.4 Oscillator strengths of *D* line components for Ge:Ga as functions of uniaxial stress along the [001] direction for (a) $\mathbf{E}_{\parallel}$ and (b) $\mathbf{E}_{\perp}$.

4.3.3 ***C-line***

The *C* line is associated with not only the $1\overline{\Gamma}_8^+ \to 1\overline{\Gamma}_7^-$ and the $1\overline{\Gamma}_8^+ \to 3\overline{\Gamma}_8^-$ transitions, but also the $1\overline{\Gamma}_8^+ \to 3\overline{\Gamma}_8^+$ transition, which is a transition between even-parity states. It is worth mentioning that although the envelope functions of an acceptor state have a common parity, the total wave function of Eq. (3.1) does not have a definite parity because of the lack of inversion symmetry in the p-Ge system. Therefore, this could allow the electric-dipole transitions between acceptor states of the same parity. For the transitions between even-parity states, the matrix element integral over all space is nearly equal to that over the central-cell region since the envelope functions are slowly varying outside the central-cell region. Therefore, the simple empirical form of the central-cell correction V_{cc} of Eq. (3.6) should not be applicable. On the contrary, for the electric-dipole transitions between acceptor states of opposite parity and between odd-parity states, the calculated results are not correlated closely with the detailed form of the V_{cc} since the wave functions of odd-parity states almost vanish in the central-cell region. This is the reason why adopting the simple empirical form of V_{cc}, we can obtain results in excellent agreement with experiments.

Figure 4.5 shows a comparison between our calculation and the experimental result of Vickers *et al*. [42] on the stress dependence of the C^* and the D^* related levels for Ge:Ga, where, as defined by Gershenzon *et al*. [45], the D^* corresponds to the $1\overline{\Gamma}_8^-$ level which splits into $2\Gamma_6^-$ and $2\Gamma_7^-$ under [001] stress. To comply with the data of Vickers, our calculated energy levels are measured from a stress-dependent energy reference $E\left(1\overline{\Gamma}_8^+\right) - P_\varepsilon$, where $E\left(1\overline{\Gamma}_8^+\right)$ is the energy level of the ground state $1\overline{\Gamma}_8^+$ at zero stress and P_ε is the strained energy induced by hydrostatic compression. Our results show excellent agreement with the experiment [42] for the odd-parity states but the relative energy position between the even

parity states (i.e., $3\Gamma_6^+$ and $3\Gamma_7^+$ states) is reversed. The reason is not clear. There is no artificial energy shift in our calculation for the data in Fig. 4.5.

In the presence of [001] stress, the $1\bar{\Gamma}_7^-$ state becomes the $3\Gamma_7^-$ state, and the $3\bar{\Gamma}_8^-$ state splits into the $3\Gamma_6^-$ and the $4\Gamma_7^-$ states. As a result, the *C* line, excluding the transitions between even-parity states, splits into six components, $C_1(1\Gamma_6^+ \rightarrow 3\Gamma_7^-)$, $C_2(1\Gamma_6^+ \rightarrow 3\Gamma_6^-)$, $C_5(1\Gamma_6^+ \rightarrow 4\Gamma_7^-)$, $C_6(1\Gamma_7^+ \rightarrow 3\Gamma_7^-)$, $C_7(1\Gamma_7^+ \rightarrow 3\Gamma_6^-)$, and $C_{10}(1\Gamma_7^+ \rightarrow 4\Gamma_7^-)$. Here, the notation of the *C* line components is the same as that of [42]. It is known that the main transition of *C* line at zero stress is $1\bar{\Gamma}_8^+ \rightarrow 1\bar{\Gamma}_7^-$ [26, 29, 44]. This can also be seen in Fig. 4.1. Therefore, the main *C* line components should be those whose final state is $3\Gamma_7^-$ at [001] infinitesimal stress. They are C_1 (for $\mathbf{E}_{\parallel}$) and C_6 (for $\mathbf{E}_{\perp}$) as can be seen in Fig. 4.6. However, since a small stress can cause a strong coupling between the $3\Gamma_7^-$ and the $4\Gamma_7^-$ states, the oscillator strengths of the *C* line components whose final states are the $3\Gamma_7^-$ and the $4\Gamma_7^-$ states change rapidly with stress when the stress is close to zero. The main *C* line component for $\mathbf{E}_{\parallel}$ ($\mathbf{E}_{\perp}$) becomes C_5 (C_{10}) when the stress is larger than 0.28 (0.02) kbar. In addition, in comparison with the coupling between the $3\Gamma_7^-$ and the $4\Gamma_7^-$ states, the couplings of the $3\Gamma_7^-$ ($4\Gamma_7^-$) state with other acceptor states should be insignificant so that the sum of the oscillator strengths of the C_1 and the C_5 components and the sum of the C_6 and the C_{10} components are not susceptible to the stress.

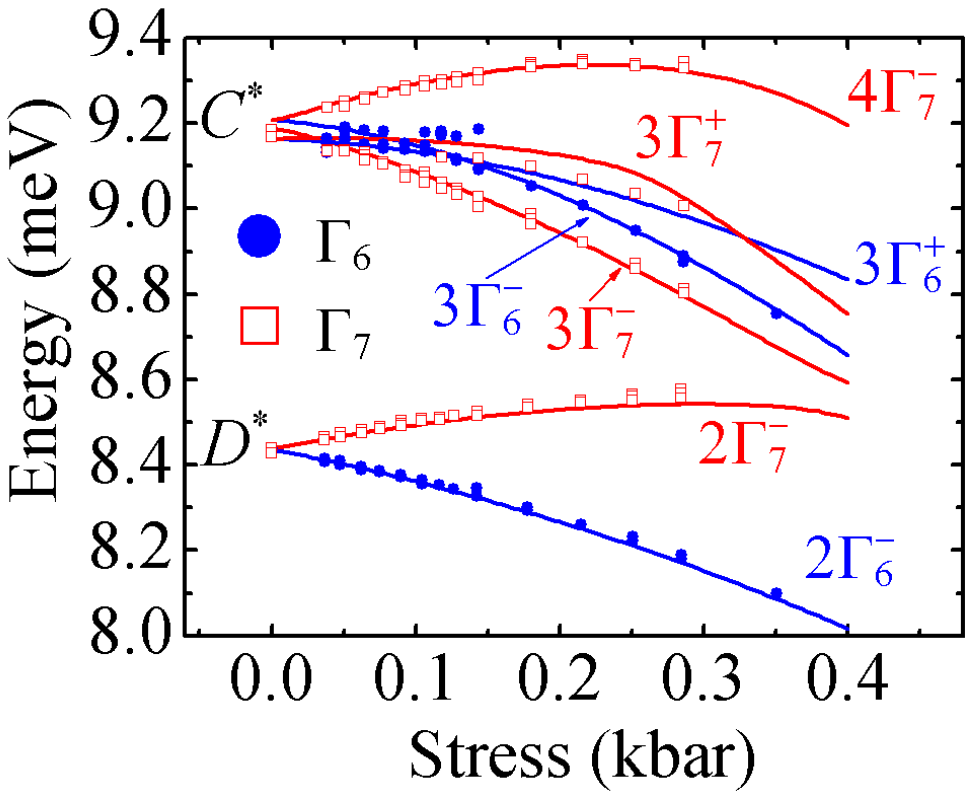

Fig. 4.5 Stress dependence of the C^* and the D^* line components for Ge:Ga. The energies are measured from a stress-dependent reference $E\left(1\bar{\Gamma}_8^+\right)-P_\varepsilon$, where $E\left(1\bar{\Gamma}_8^+\right)$ is the energy level of the ground state $1\bar{\Gamma}_8^+$ at zero stress and P_ε is the strained energy induced by hydrostatic compression. The solid lines are the results of the present work. The solid circles (open squares) denote the experimental data associated with the Γ_6 (Γ_7) final states taken from [42].

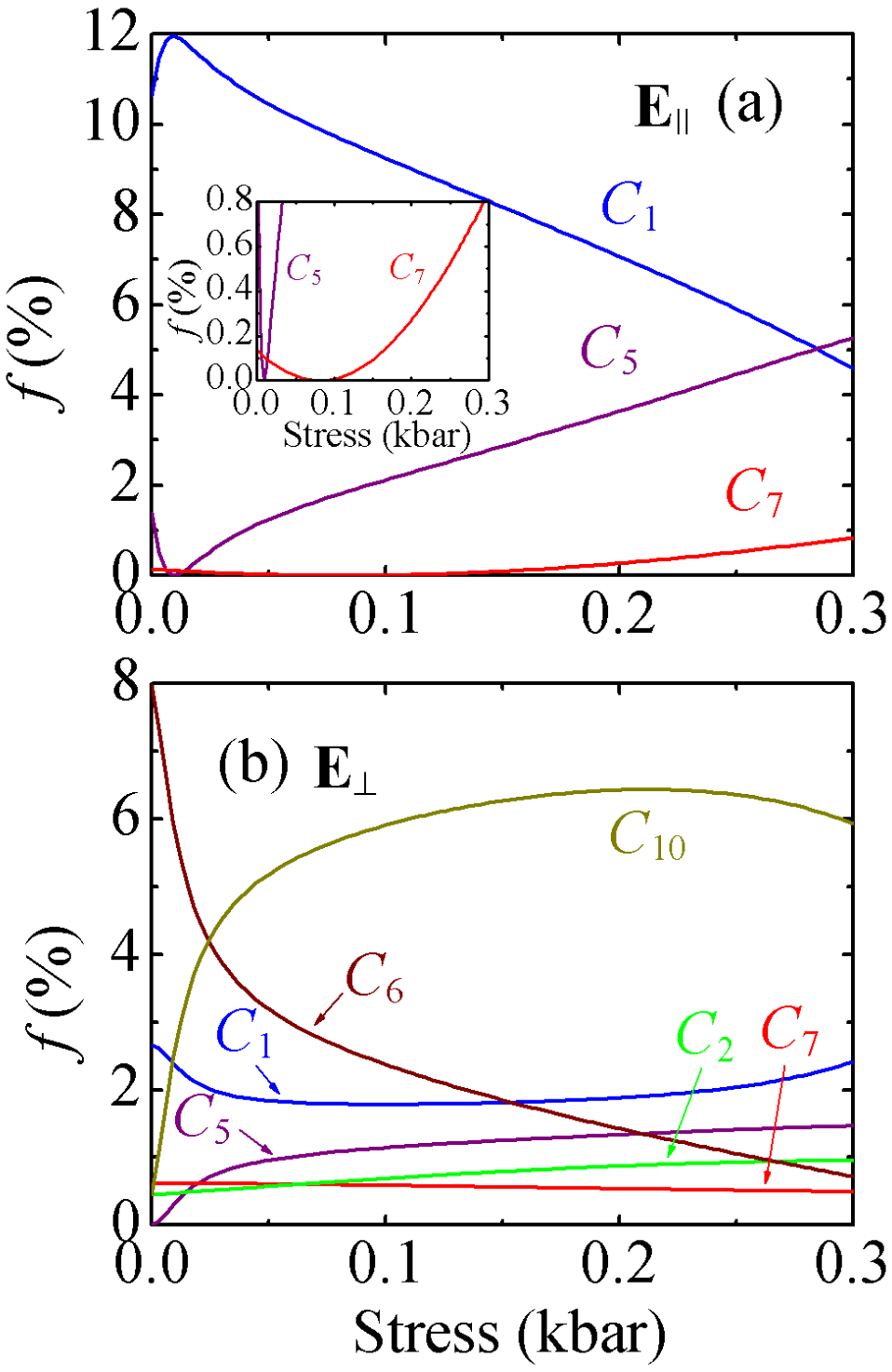

Fig. 4.6 Oscillator strengths of *C* line components for Ge:Ga as functions of uniaxial stress along the [001] direction for (a) $\mathbf{E}_{\parallel}$ and (b) $\mathbf{E}_{\perp}$.

4.3.4 ***B-line***

In the presence of [001] stress, the *B* line transition $1\bar{\Gamma}_8^+ \rightarrow 4\bar{\Gamma}_8^-$ splits into four components. As shown in Fig 3.3, Dickey and Dimmock [49] measured the transition energies of two of the four *B* line components for Ge:In as functions of stress and we assigned the two components to the $1\Gamma_6^+ \rightarrow 5\Gamma_7^-$ (denoted by B_2) and the $1\Gamma_7^+ \rightarrow 4\Gamma_6^-$ (denoted by B_3) transitions. Figure 4.7 shows the stress dependence of the oscillator strengths of the *B* line components for Ge:In. As can be seen, the $B_1(1\Gamma_6^+ \rightarrow 4\Gamma_6^-)$ and the $B_4(1\Gamma_7^+ \rightarrow 5\Gamma_7^-)$ components are forbidden for $\mathbf{E}_{\parallel}$, and their oscillator strengths for $\mathbf{E}_{\perp}$ are smaller than those of the B_2 and the B_3 components in the low-stress region (<0.14 kbar). This is in agreement with the fact that only the B_2 and the B_3 components were observed in the experiment of [49]. At the stress close to 0.14 kbar, the oscillator strength of the B_2 component changes dramatically with stress due to the anticrossing between the $5\Gamma_7^-$ and the $6\Gamma_7^-$ states. Therefore, the B_2 component should be assigned to the $1\Gamma_6^+ \rightarrow 6\Gamma_7^-$ transition when the stress is higher than 0.14 kbar.

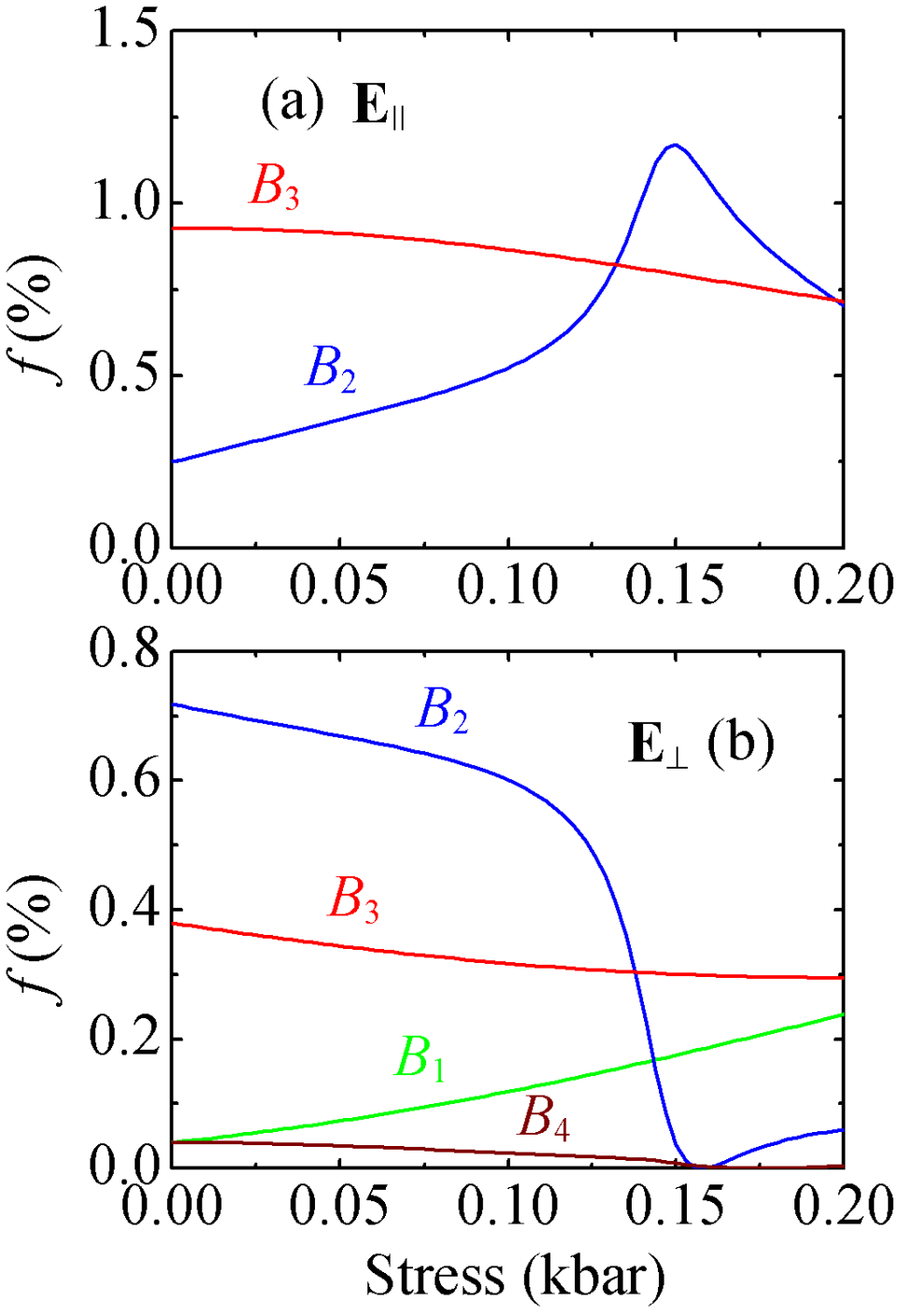

Fig. 4.7 Oscillator strengths of *B* line components for Ge:Ga as functions of uniaxial stress along the [001] direction for (a) $\mathbf{E}_{\parallel}$ and (b) $\mathbf{E}_{\perp}$.

4.3.5 ***Absorption Spectra***

Figure 4.8 shows the calculated absorption spectra for Ge:Ga at liquid-temperatue (T=4.22 K). In the calculation, the acceptor concentration is taken to be 6×10^{13} cm^{-3}, and the stress for panel (a) and (b) is taken to be 0.078 and 0.22 kbar, respectively, as the same parameters in [42]. We also replace the delta function in Eq. (3.11) with a Lorentzian line-shape function whose full width at half-maximum (FWHM) is taken to be 0.25 cm^{-1}. Here, the B_2 component is assigned to the $1\Gamma_6^+ \rightarrow 5\Gamma_7^-$ transition in panel (a) and to the $1\Gamma_6^+ \rightarrow 6\Gamma_7^-$ transition in panel (b) due to the anticrossing between the $5\Gamma_7^-$ and the $6\Gamma_7^-$ states as mentioned previously. As can be seen, except for the presence of the transitions between even-parity states, the calculated spectra are in good agreement with the experimental results, and successfully predict that the C_7 component for $\mathbf{E}_{\|}$ vanishes at 0.078 kbar but appears at 0.22 kbar. This can also be understood in terms of the stress dependence of the C_7 oscillator strength for $\mathbf{E}_{\|}$ in Fig. 4.6(a).

In panel (b), the transition energies of D_3 (69.4 cm^{-1}), C_1 (69.2 cm^{-1}), and C_2 (69.9 cm^{-1}) components are very close to each other, and the C_1 and C_2 components are much weaker than the D_3 component so that the D_3, C_1, and C_2 components are not resolved by experiment. In addition to the C_7, C_{10}, B_2, and B_3 components, there are fourteen transition lines with transition energies between 75 cm^{-1} and 80 cm^{-1}. These transitions, whose initial state is $1\Gamma_6^+$, are not labelled in panel (b) because they are too weak to be observed.

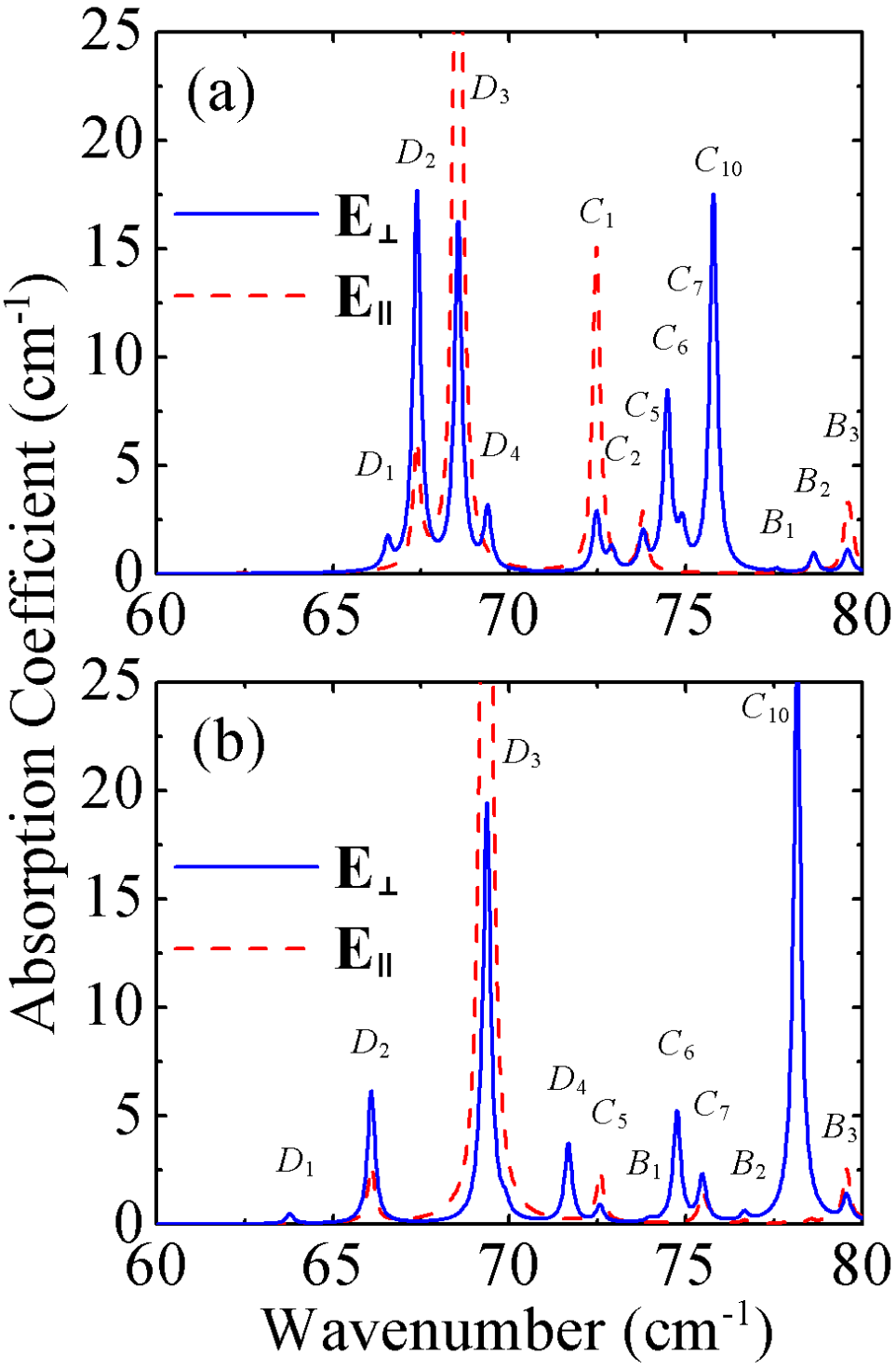

Fig. 4.8 Absorption spectra for Ge:Ga under [001] stress of (a) 0.078 kbar and (b) 0.22 kbar at liquid-helium temperature (T=4.22 K). The acceptor concentration is 6×10^{13} cm^{-3}. Each peak of the spectra is broadened by a Lorentzian line-shape function with a FWHM of 0.25 cm^{-1}.

4.4 **Effect of Stress on the Electronic structure**

4.4.1 ***Isocoric acceptor Ga in Ge***

We have considered the case of low-stress region (≤0.3 kbar). In this section, we will discuss the general features of the stress dependence on the acceptor electronic structure. Here, the discussion is not limited to the case of low-stress region, in which the final states of the *G*, *D*, and *C* line components do not either cross or anticross.

Figures 3.9 and 3.10 show the binding energies of even- and odd-parity states, respectively, for Ge:Ga as functions of uniaxial stress along the [001] direction. The panels (b) of the two figures are zoom-in of panels (a) so that the curves of several excited states of low binding energy are distinguishable. A positive (negative) stress means a compressive (tensile) stress. The binding energy of an acceptor state is the minimum energy required to liberate a hole bound at the state, that is, the difference in energy between the state and the nearest valence band edge. Since the valence band edges vary with the stress, we calculate and plot the edges of the HH, the LH, and the SO bands as functions of [001] stress in Fig. 4.11 for convenience in later analysis. With the compressive stress, the LH (HH) band edge moves monotonically upwards (downwards), while with tensile stress the HH (LH) band edge moves upwards (downwards). Accordingly, we have $E_{\mathrm{B}}\left(n\Gamma_i^u\right)=E\left(n\Gamma_i^u\right)-E_{\mathrm{LH}}$ for compressive stress and $E_{\mathrm{B}}\left(n\Gamma_i^u\right)=E\left(n\Gamma_i^u\right)-E_{\mathrm{HH}}$ for tensile stress, where $E_{\mathrm{B}}\left(n\Gamma_i^u\right)$ is the binding energy of the $n\Gamma_i^u$ state, and E_{LH} and E_{HH} are the LH and the HH band edges, respectively.

As shown in Figs. 3.9 and 3.10, the binding energies are susceptible to the stress as the stress is lower than 3 kbar but become more insensitive to the stress as the stress is larger. Such stress dependence is related to the composition of the acceptor states. As the stress is low ($\lesssim$ 3 kbar), the states are composed in a manner that the HH composition f_{HH} and the LH

composition f_{LH} are both significant but the SO composition is negligible since $E\left(n\Gamma_i^u\right)-E_{HH} \approx E\left(n\Gamma_i^u\right)-E_{LH} \ll E\left(n\Gamma_i^u\right)-E_{SO}$, where E_{SO} is the edge of the SO band. As compression increases, some higher-energy levels move downwards with the HH band and finally become resonant in nature after merging into the LH band. The other levels which remain above the LH band do not move with the HH band. As a result, the ratio f_{HH}/ f_{LH} decreases with compression for the bound states because of the increase of $E\left(n\Gamma_i^u\right)-E_{HH}$. As the stress is sufficiently large such that $E\left(n\Gamma_i^u\right)-E_{HH} \gg E\left(n\Gamma_i^u\right)-E_{LH}$, the bound states are almost of LH character (i.e., $f_{LH} \approx 1$ and $f_{HH} \approx 0$). In the light of the variational principle, more basis functions are preferred at low stress to form the eigenfunctions of acceptor states than at high stress. This explains the facts that the binding energy is largest at zero stress and decreases rapidly with low stress but changes slowly with high stress. The situation of tensile stress is similar to that of compression, but with the roles of HH and LH replacing each other. Analogously, under a sufficiently high tensile stress, the acceptor states are almost of HH character. An exception occurs in the high-stress region where the binding energy slightly increases with compressive stress but slightly decreases with tensile stress. This is because at a high stress the HH-LH coupling in the acceptor states becomes unimportant and the effective mass is the dominant factor in the stress dependence of binding energy. The LH mass is increased by compressive stress but the HH mass is reduced by tensile stress.

There is a substantial difference in stress dependence of binding energy between the low-energy even-parity states and the low-energy odd-parity states as the stress is lower than 3 kbar. As shown in Figs. 3.9 and 3.10, the binding energy of the $1\Gamma_6^+$ ($1\Gamma_7^+$) state decreases much more rapidly with the compressive (tensile) stress than with the tensile (compressive) stress but such asymmetry does not appear so remarkably for the odd-parity states. To realize the difference, it is instructive to invoke the correlation between the HH-LH coupling and the

binding energy of an acceptor state. Figure 4.12 shows the HH composition f_{HH} and the LH composition f_{LH} of Ge:Ga acceptor states $1\Gamma_6^+$ in (a), $1\Gamma_7^+$ in (b), $1\Gamma_6^-$ in (c), and $1\Gamma_7^-$ in (d) as functions of [001] stress. The SO composition is negligibly small (less than 0.3%) and hence not shown here. We find from Fig. 4.12(a) that f_{HH} =75% and f_{LH} =25% for the $1\Gamma_6^+$ state at zero stress, indicating that the $1\Gamma_6^+$ state is like HH more than like LH in character. The compositions of the $1\Gamma_6^+$ state change rapidly with the compressive stress but much more slowly with the tensile stress as the stress is lower than 3 kbar. At a compressive stress above 3 kbar, the $1\Gamma_6^+$ state becomes almost of LH character (f_{HH} ≈0 and f_{LH} ≈100%) while for tensile stress it remains HH-like. At a tensile stress of 3 kBar, the $1\Gamma_6^+$ state does not become a purely HH-like state, but still contains a LH composition of about 10%. Such a rapid change in composition is the cause of the rapid reduction in binding energy with the compressive stress. For the $1\Gamma_7^+$ state, the situation is reverse. As seen from Fig. 4.12(b), the $1\Gamma_7^+$ state is LH-like with f_{LH} =75% at zero stress. It turns out to become almost purely HH-like after a rapid change in composition with the tensile stress, but remains still LH-like as its f_{LH} value increases slowly with the compressive stress. For the $1\Gamma_6^-$ ($1\Gamma_7^-$) state, as shown in Fig. 4.12(c) and (d), f_{LH} =55%> f_{HH} (f_{HH} =55%> f_{LH}) at zero stress. This causes the binding energy of the $1\Gamma_6^-$ ($1\Gamma_7^-$) state to decrease with the tensile (compressive) stress more rapidly than with the compressive (tensile) stress, as Fig. 4.10 shows. The asymmetry in the stress dependence for the odd-parity states is not as prominent as for the even-parity states due to the small difference between f_{LH} and f_{HH} at zero stress.

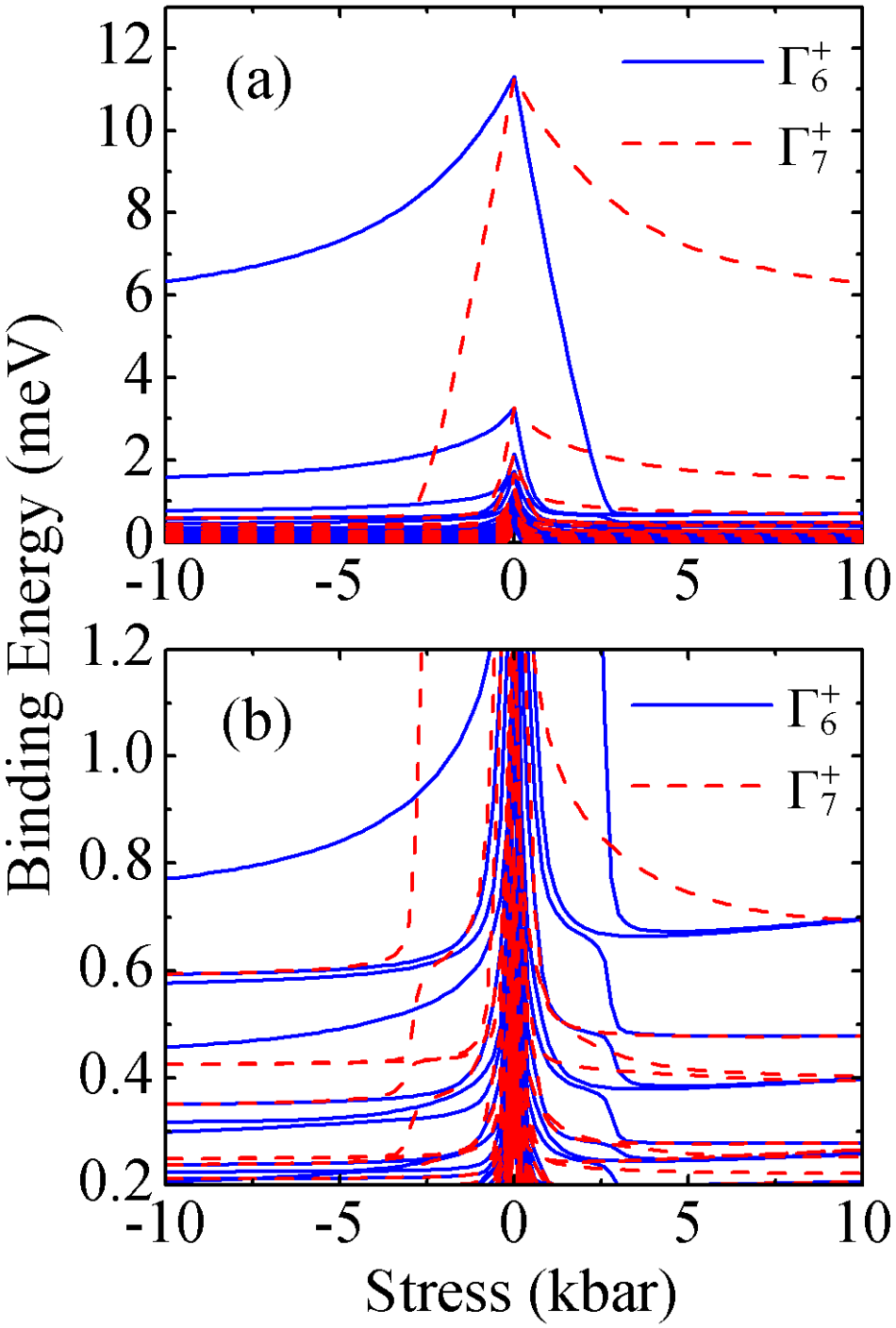

Fig. 4.9 Binding energies of even-parity states as functions of uniaxial stress along the [001] direction for Ge:Ga. The positive (negative) stress means a compressive (tensile) stress. The panel (b) is a zoom-in of the panel (a).

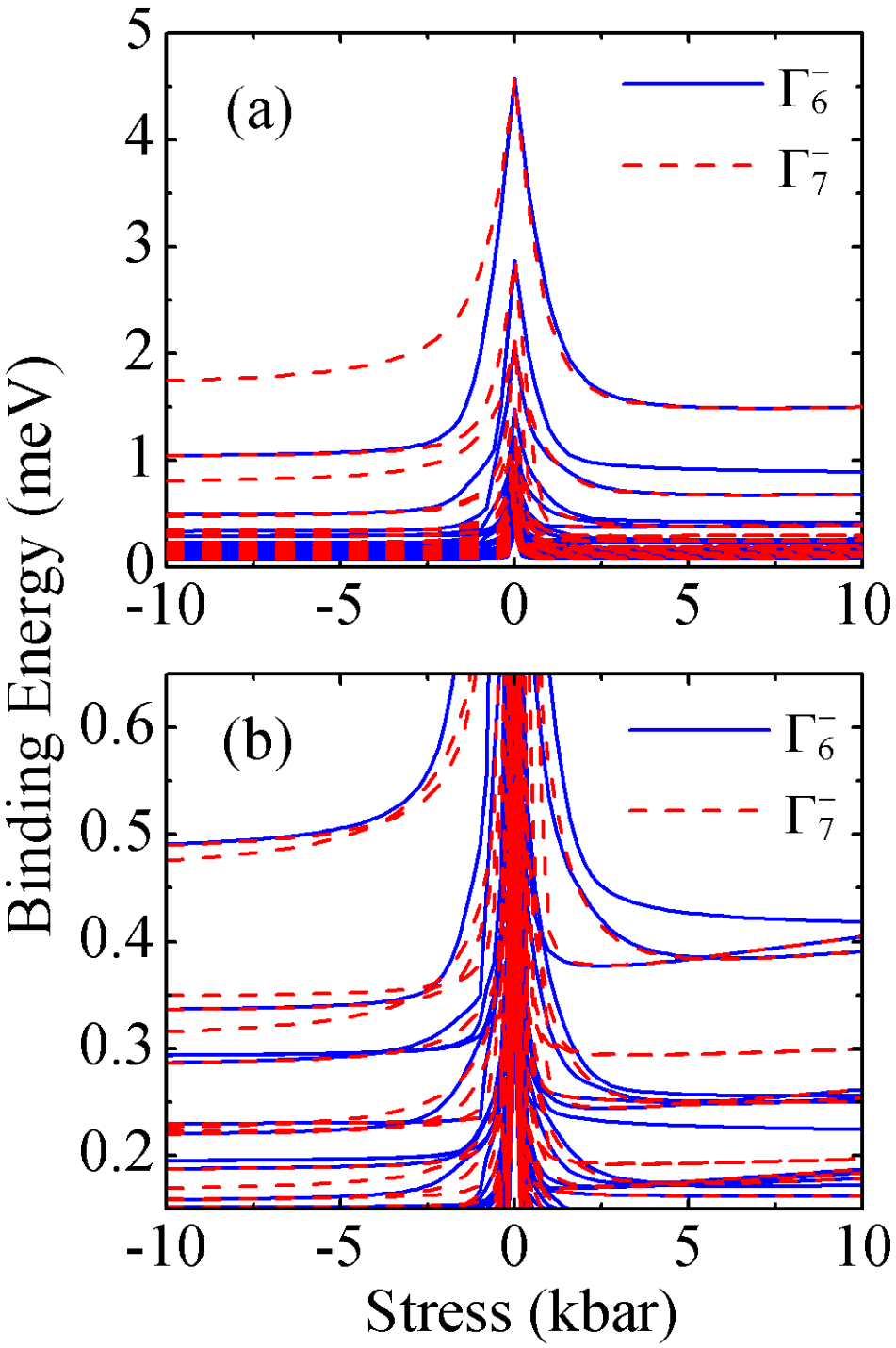

Fig. 4.10 Binding energies of odd-parity states as functions of uniaxial stress along the [001] direction for Ge:Ga. The positive (negative) stress means a compressive (tensile) stress. The panel (b) is a zoom-in of the panel (a).

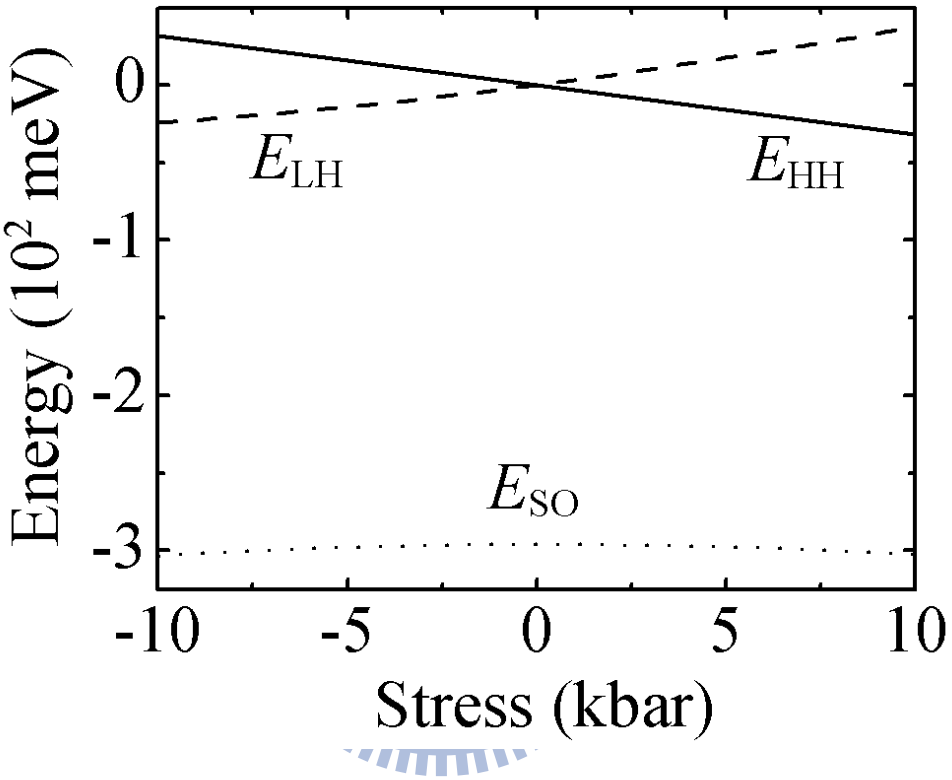

Fig. 4.11 The HH, LH, and SO band edges (denoted by E_{HH}, E_{LH}, and E_{SO}, respectively) as functions of uniaxial stress along the [001] direction for Ge:Ga. The positive (negative) stress means a compressive (tensile) stress.

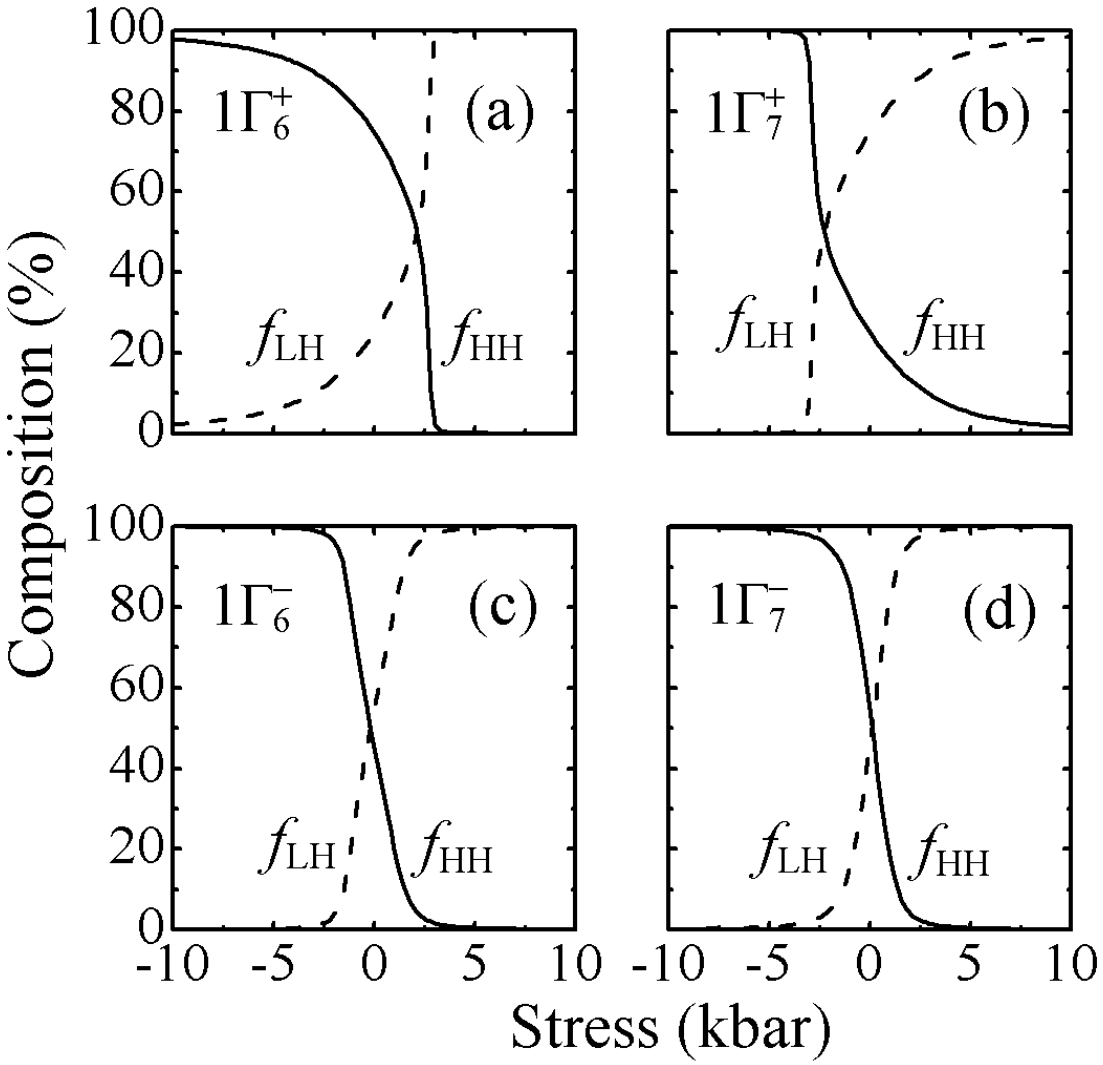

Fig. 4.12 Stress dependence of the HH composition (f_{HH}) and the LH composition (f_{LH}) of (a) $1\Gamma_6^+$, (b) $1\Gamma_7^+$, (c) $1\Gamma_6^-$, and (d) $1\Gamma_7^-$ for Ge:Ga. The positive (negative) stress means a compressive (tensile) stress.

4.4.2 ***Chemical Shifts of various species of group-III acceptors***

In section 3.1, we have presented the energy levels of even-parity states for the nonisocoric group-III acceptors in strainless Ge. In the previous section, we have also discussed the energy levels of even-parity states for the nonisocoric group-III acceptors in strainless Ge. Now we are going to explore the stress effect on the energy levels of even-parity states for various nonisocoric group-III acceptors in Ge. Figure 4.13 shows the chemical shifts of several low-energy even-parity states versus [001] stress for nonisocoric acceptors B, Al, In, and Tl, as well as the isocoric acceptor Ga, doped in Ge. The chemical shift of a state for a certain species of acceptor is defined as the deviation of the energy level of the state from the corresponding level which is obtained by setting the central-cell correction V_{cc} at zero (i.e., A=0). It is caused by the central-cell correction which has been included in Eq. (3.6). Due to the short-range nature of the central-cell potential, the chemical shift can be considered to be proportional nearly to the value of A times the probability density of the hole at the acceptor site. Since only the s (l=0) composition of the wave function contributes probability at the acceptor site, the chemical shift should be proportional approximately to $A\sum_{j=1}^{6}\left|g_{j00}(0)\right|^2$. As a result, the chemical shifts for Ga are negligibly small, as can be seen from Fig. 4.13, because of the small value of A. Also, the chemical shifts for B and Al are positive and those for In and Tl are negative in accordance with the signs of their A values, which reflects a positive or negative change in the effective force on the hole exerted by the core states. However, the chemical shift does not linearly depend on A. As mentioned in section 3.1, the negative A enhances the total attractive force of the acceptor acting on the hole and causes the wave functions to be more localized around the acceptor site than a positive A. As a result, the chemical shift for Tl is more predominant than for B although the A value for Tl is smaller in magnitude. For In, the chemical shift can be comparable to that for B although the magnitude of A is

only about one half of that for B.

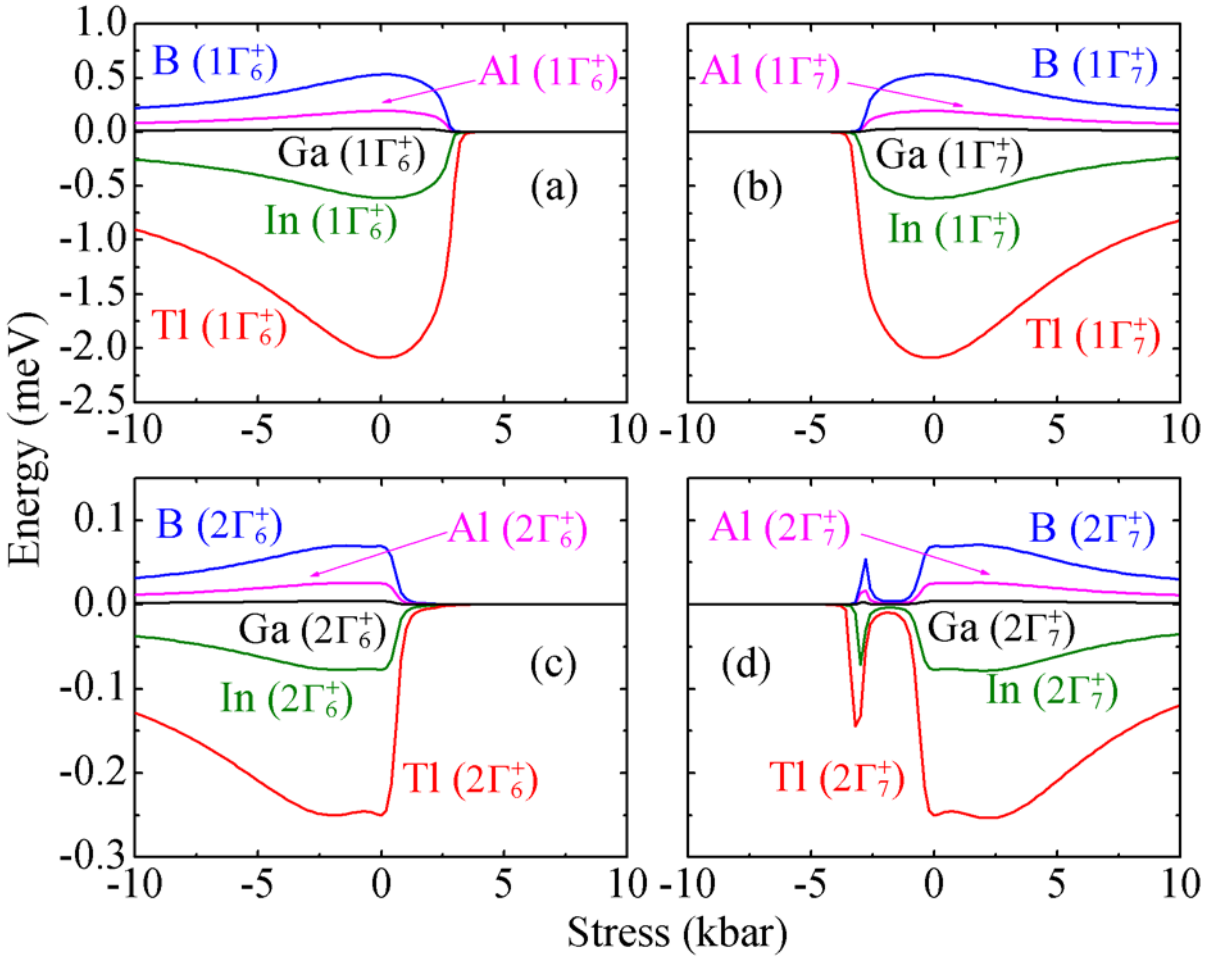

Fig. 4.13 Chemical shifts of (a) $1\Gamma_6^+$, (b) $1\Gamma_7^+$, (c) $2\Gamma_6^+$, and (d) $2\Gamma_7^+$ as functions of [001] stress for various group-III acceptors in Ge. The positive (negative) stress means a compressive (tensile) stress.

4.5 **High-Stress Region**

4.5.1 ***Features in the high-stress region***

The acceptor states in the presence of [001] stress are doubly degenerate except for the case of accidentally degeneracy. However, as mentioned earlier, the HH-LH coupling is negligible when the stress is sufficiently high. Such decoupling of the HH and LH can cause extra degeneracy of the acceptor states as can be seen in Fig. 4.9 and 4.10. In this case, the effective-mass Hamiltonian has nearly azimuthal symmetry and the acceptor states can be regarded as belonging to a single valence band. Therefore, the acceptor states can be expressed as

$$\left|\Psi^{u}_{JMm}\right\rangle = \sum_{l\geq m}^{(u)} g_{JMlm} Y_{lm}(\theta,\phi)\left|JM\right\rangle, \tag{4.1}$$

with *J*, *M*, *m*, and *u* as good quantum numbers, where *u* is the parity of the envelope function. The sum in Eq. (4.1) runs over even *l* for even-parity states (*u*≡+), and runs over odd *l* for odd-parity states (*u*≡–). The azimuthal and the time-reversal symmetries ensure the fourfold degeneracy in the states $\left|\Psi^{u}_{JMm}\right\rangle$, $\left|\Psi^{u}_{J,M,-m}\right\rangle$, $\left|\Psi^{u}_{J,-M,m}\right\rangle$, and $\left|\Psi^{u}_{J,-M,-m}\right\rangle$ for *m*≠0, and the twofold degeneracy in the states $\left|\Psi^{u}_{JM0}\right\rangle$ and $\left|\Psi^{u}_{J,-M,0}\right\rangle$ for *m*=0. There are three possible combinations in the high-stress case for the extra degeneracy, $\Gamma^{u}_{6}+\Gamma^{u}_{7}$, $2\times\Gamma^{u}_{6}$, and $2\times\Gamma^{u}_{7}$ for *m*≠0, and no extra degeneracy for *m*=0. The combinations depend on the values of *m*, *u*, and *M*, and are listed in Table 4.4. For HH-like states (*M*=±3/2), the representations without extra degeneracy are Γ^{+}_{6} and Γ^{-}_{7} for *m*=0, and the combinations with extra degeneracy include (i) $\Gamma^{\pm}_{6}+\Gamma^{\pm}_{7}$ for |*m*|=2*n*–1, (ii) $2\times\Gamma^{+}_{6}$ and $2\times\Gamma^{-}_{7}$ for |*m*|=4*n*, and (iii) $2\times\Gamma^{-}_{6}$ and $2\times\Gamma^{+}_{7}$ for |*m*|=4*n*–2, where *n* is a positive integer. For LH-like states (*M*=±1/2), the possible degeneracies can be obtained from those for the HH-like states just by interchanging the parities + and –. The results for the LH-like states are also listed in Table 4.4. We emphasize that

only the Γ_7^+ and the Γ_6^- states (the Γ_6^+ and the Γ_7^- states) can remain doubly degenerate without extra degeneracy at high compressive (tensile) stress, in agreement with the results in Fig. 4.9 and 3.10.

We know from Table 4.4 the asymptotic property that the Γ_6^+ (Γ_7^+) states have no significant m=0 component at high compressive (tensile) stress. Therefore, the s compositions of the Γ_6^+ (Γ_7^+) states decrease to zero with the compressive (tensile) stress. This can explain the asymmetric stress dependence of the chemical shift in Fig. 4.13 wherein the magnitude of the chemical shift for the Γ_6^+ (Γ_7^+) states decreases to almost zero with the compressive (tensile) stress much more rapidly than with the tensile (compressive) stress. On the other hand, the relatively mild stress dependence for the Γ_6^+ (Γ_7^+) states in the high tensile (compressive) stress region is caused by the distortion of the wave functions whose s composition reduce with the deformation.

Even though the index l in Eq. (4.1) is not a good quantum number, we found, by the calculation of l compositions as functions of stress, that only the acceptor states close to the anticrossing point can have different non-negligible l compositions for the ground state and the odd-parity states. Therefore, the l can approximately be regarded as a good quantum number in the high-stress region. In Fig. 4.14, we use nX_m to denote the odd-parity acceptor states in the compressive high-stress region. Here, X denotes a lower-case letter for the angular momentum l (s, p, d, f, … for l=0,1,2,3,…, respectively), and n is a positive integer for sort of the acceptor states with the same l and m according to their energy levels. As can be seen, the result is consistent with Table 4.4, and the nX_m and the nX_{-m} states are degenerate in the high-stress region.

The decoupling of the HH and LH can cause not only the extra degeneracy of the accep-

tor states but also additional selection rules of the electric-dipole transitions. Figure 4.15 shows the stress dependence of oscillator strengths of electric-dipole transitions from the ground state $1\Gamma_7^+$ to the odd parity states. The results agree with the selection rules of the electric-dipole transitions: $\Delta l=\pm 1$, $\Delta m=0$, for $\mathbf{E}_{\|}$ and $\Delta l=\pm 1$, $\Delta m=\pm 1$, for $\mathbf{E}_{\perp}$. In the high-stress region, the ground state is s-like. Therefore, for $\mathbf{E}_{\|}$ ($\mathbf{E}_{\perp}$), only the transitions whose final states are np_0 ($np_{\pm 1}$) can have non-negligible oscillator strengths. In addition, as mentioned in section 3.3.1, the *G* line components are weak in the low-stress region because of the appreciable d composition of the $1\Gamma_6^+$ and the $1\Gamma_7^+$ states. However, with the increase of stress, the d (s) composition of $1\Gamma_7^+$ decreases (increases) so that for $\mathbf{E}_{\perp}$, the oscillator strengths of the G_3 and G_4 components, which correspond to the $1\Gamma_7^+ \rightarrow 2p_{\pm 1}$ transitions in the high-stress region, increase with stress, and hence the $1\Gamma_7^+ \rightarrow 2p_{\pm 1}$ transitions become the main transitions in the high-stress region.

4.5.2 ***Justification of the model potential in the high-stress region***

We have shown that our calculated results are in excellent agreement with experiment up to 0.35 kbar. However, we do not find high-stress experimental data in the literature to confirm the validity of our calculation, in which the stress is up to 10 kbar. In fact, the so-called high stress of 10 kbar gives the normal strain ε_z along the uniaxial axis as small as –0.97% for Ge. Therefore, the Bir-Pikus effective-mass theory [36] is still applicable and other stress effects should give a negligible higher-order correction. For instance, we have supposed the functional form of the semi-empirical impurity potential *V* introduced in Eq. (3.6) to be independent of the stress in the calculation. To justify the assumption, we reconsider the impur-

ity potential as contributed from two parts [21]. One is called the bare potential V_b, which is caused by the difference in the charges of the closed-shell ions (namely, the nuclei plus the core electrons) between the crystals with and without the impurity present. The other one is caused by the redistribution of valence electrons due to the presence of the impurity and is called the screening potential V_s since, from the viewpoint of the hole of interest, the valence electrons play a role of screening the bare potential. It is reasonable to assume the inner states of all the closed-shell ions to be unaffected by the presence of the impurity, except for the state of the host ion to be replaced by the impurity ion. As a result, the presence of the impurity gives a bare potential as the Coulomb potential due to a point charge at the impurity site. Furthermore, the stress as small as we have considered should not alter significantly the inner states of the host and the impurity ions. Neglecting the lattice relaxation due to the presence of the impurity, we conclude that the strain causes a change only in the screening potential, in addition to the deformation of the lattice which has been considered by the Bir-Pikus theory.

The q-dependent dielectric screening of the impurity potential in Eq. (3.6) is based on the assumptions that the distribution of valence electrons responds linearly to the presence of the impurity and that the Umklapp elements of the dielectric tensor are neglected [25]. According to our previous argument, the assumptions should be valid regardless of the applied stress we have considered. In other words, the functional form of the impurity is applicable not only for low stress (<0.35 kbar), as has been confirmed by the observed transition energies, but also for stress up to 10 kbar if we allow the dielectric constant ϵ to be a function of the stress.

As has been pointed out, the correction due to the stress dependence of ϵ should be small compared to the Bir-Pikus strain effect. Goi *et al*. [50] have measured the stress dependence of ϵ for Ge at room temperature, giving

$$\epsilon\left(P, T = 300\ \mathrm{K}\right) = 15.94 - 0.36P + 0.014P^2, \tag{4.2}$$

where P is the hydrostatic stress (in unit of 10 kbar). To obtain an expression for low temper-

ature, we suppose the variation of temperature also gives a small effect on ϵ such that the ϵ can be expressed as a separable function of P and T, namely, a function in a product of functions only of P and only of T. Accordingly, the dielectric constant at T=0 K is

$$\begin{aligned}\epsilon(P,T=0\text{ K}) &= \epsilon(0,0\text{ K})\epsilon(P,300\text{ K})/\epsilon(0,300\text{ K}) \\ &= 15.36-0.347P+0.0135P^2\end{aligned} \tag{4.3}$$

where we have used ϵ (0,0 K)=15.36 [43]. As expected, we see that the stress dependence of ϵ is small for the stress up to 10 kbar. For the uniaxial stress σ along the [001] direction in our case, the stress dependence of ϵ can be obtained from Eq. (4.3) by replacing the coefficient in the linear-in-P term with its one-third and neglecting the last term. This results in $\epsilon(\sigma)$=15.36–0.116σ. It gives correction no more than 2.2% for the energy levels and correction no more than 4.6% for the chemical shifts for a stress of 10 kbar.

Table 4.4 Combinations of two-dimensional representations for extra dengeneracy, if possible, in the limiting case of high stress. They depend on the Bloch function $|JM\rangle$, the magnetic quantum number *m*, and the parity. The *n* is a positive integer.

		Combinations	
$\lvert J, M\rangle$	$\lvert m\rvert$	Even-Parity States	Odd-Parity States
$\lvert\frac{3}{2}, \pm\frac{3}{2}\rangle$	0	Γ_6^+	Γ_7^-
	$2n-1$	$\Gamma_6^+ + \Gamma_7^+$	$\Gamma_6^- + \Gamma_7^-$
	$4n$	$2 \times \Gamma_6^+$	$2 \times \Gamma_7^-$
	$4n-2$	$2 \times \Gamma_7^+$	$2 \times \Gamma_6^-$
$\lvert\frac{3}{2}, \pm\frac{1}{2}\rangle$	0	Γ_7^+	Γ_6^-
	$2n-1$	$\Gamma_6^+ + \Gamma_7^+$	$\Gamma_6^- + \Gamma_7^-$
	$4n$	$2 \times \Gamma_7^+$	$2 \times \Gamma_6^-$
	$4n-2$	$2 \times \Gamma_6^+$	$2 \times \Gamma_7^-$

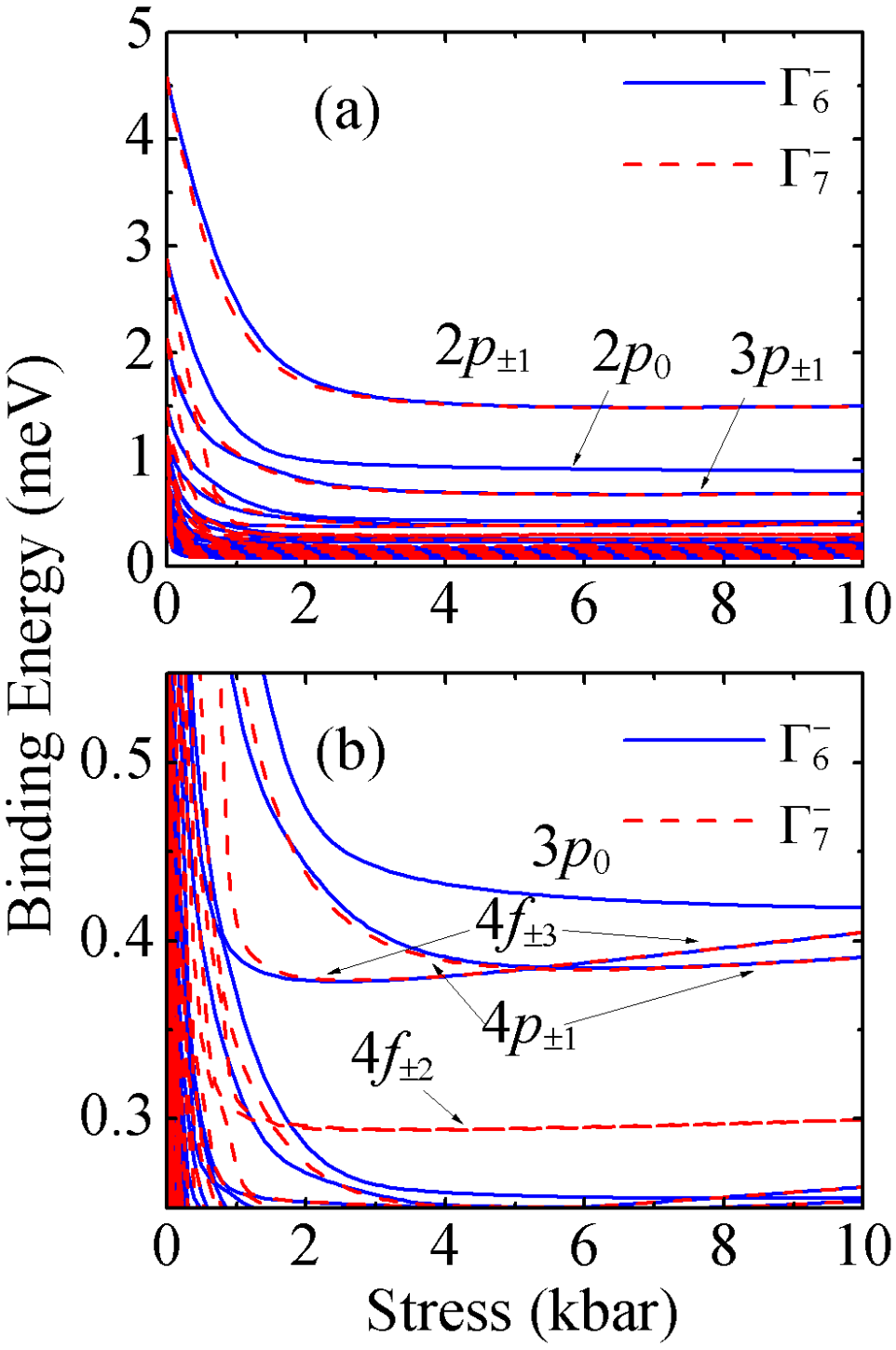

Fig. 4.14 Binding energies of odd parity states as functions of the compressive stress along the [001] direction for Ge:Ga. Panel (b) is a zoom-in of panel (a). The notation of acceptor states is explained in text.

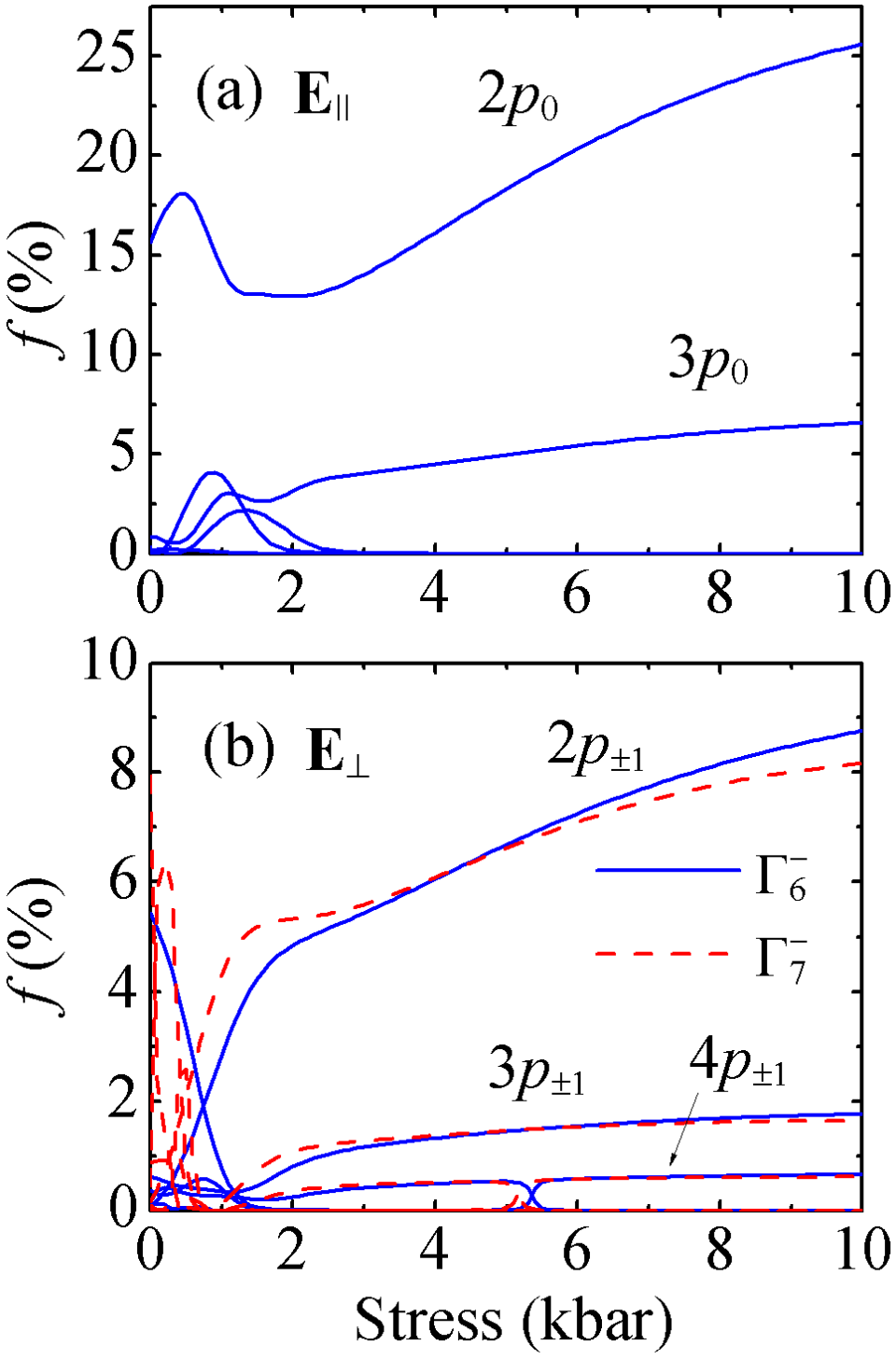

Fig. 4.15 Oscillator strengths of electric-dipole transitions from the ground state $1\Gamma_7^+$ to the odd parity states for Ge:Ga as functions of uniaxial stress along the [001] direction for (a) $\mathbf{E}_{\|}$ and (b) $\mathbf{E}_{\perp}$. The transitions which have non-negligible oscillator strengths in the high-stress region are denoted by its final states with the same notation as in Fig. 4.14.

4.6 **Summary**

We have studied the electronic structures of various group-III acceptors in Ge and the electric-dipole transitions between the acceptor states in the absence and presence of a [001] stress. We systematically discussed the cases of zero, infinitesimal, low, and high stress. Our calculated results show quantitative agreement with the available experimental spectrum so that the corresponding transition lines can be properly assigned. At zero stress, the binding energy of the ground states and the oscillator strengths of electric-dipole transitions from the ground state to the odd-parity states are more susceptible to the attractive central-cell force (e.g. for acceptor Tl) than to the repulsive one (e.g. for acceptor B). For the case of infinitesimal stress, we have calculated the intensity parameters, *u* and *v*, of transitions $1\Gamma_8^+ \rightarrow 1\Gamma_8^-$ for various species of group-III acceptors in Ge. Except for the *G* line transition, the intensity parameters are not significantly correlated with the species of acceptor atoms. At finite stress, the intensity parameters are no longer applicable due to the strain-induced couplings between acceptor states of the same symmetry. In fact, the oscillator strengths of certain transitions change appreciably even though only a small stress (<0.3 kbar) is applied. The stress effect on the binding energies of acceptor states has been found to be related to the compositions of the states. Our results show that the binding energies decrease rapidly with the stress as the stress is smaller than 3 kbar. Also, the binding energies of even-parity states exhibit remarkable asymmetry in the stress dependence due to the large difference between the HH and the LH compositions of the states. They decrease much more rapidly with compressive stress than with tensile stress for Γ_6^+ states, but conversely for Γ_7^+ states. Increasing stress results in HH-LH decoupling. The acceptor states asymptotically approach pure LH (HH) states with the compressive (tensile) stress. In the high-stress region (>3 kbar), the *l* and *m* can approximately be regarded as good quantum numbers. The nX_m and the nX_{-m} are almost degenerate.

The selection rules are $\Delta l=\pm 1$, $\Delta m=0$, for $\mathbf{E}_{\parallel}$ and $\Delta l=\pm 1$, $\Delta m=\pm 1$, for $\mathbf{E}_{\perp}$. Because the ground state becomes s-like, only the transitions to the $n\mathrm{p}_0$ ($n\mathrm{p}_{\pm 1}$) states for $\mathbf{E}_{\parallel}$ ($\mathbf{E}_{\perp}$) can have non-negligible oscillator strengths. For the same reason, the G_3 and G_4 components, which are weak in the low-stress region, become the main transitions for $\mathbf{E}_{\perp}$ in the high-stress region. The central-cell correction is important for energy levels of nonisocoric acceptors and causes significant chemical shift for even-parity states, especially for the $1\Gamma_6^+$ and the $1\Gamma_7^+$ states. The compressive (tensile) stress can reduce effectively the chemical shift of the Γ_6^+ (Γ_7^+) states because of the rapid reduction of the s component with the stress. Because of the lack of experimental data available for comparison in the high-stress region, a detailed argument has been made supporting the applicability of our calculation scheme to the case of high stress.

Part II.

Parabolic Quantum Well Laser with Heterogeneous Cavities

Chapter 5

Basic Principle and Theoretical Model

5.1 Introduction

Parabolic quantum wells (PQW) have been demonstrated to be a candidate of the active region for THz emission [51-52]. The emission efficiency depends on the ratio of the radiative to the nonradiative rates of ISB processes. The radiative transition rate is the sum of the spontaneous and the stimulated emission rates. The former is typically of the order of 10^4 to 10^5 s^{-1}. It is much less than the ISB acoutic phonon scattering rate (~10^9 s^{-1}) and the ISB optical phonon scattering rate (~10^{12} s^{-1}). Therefore, almost all the energy of carriers is dissipated through the nonradiative ISB transition and is converted into heat if there is no appropriate cavity. The THz photonic crystal (PC) metal-metal (MM) cavity containing a two-demensional (2D) metallic array can have a quality factor of (Q~50) comparable with those of micro-disk cavities [53]. Such a cavity, when incorporated with a resonant phonon quantum cascade active region, has been demonstrated to achieve THz surface-emitting lasing with narrow-beam and high-power (~1 W/cm^2) output at low temperatures (below 10 K) [54]. In the present research, we propose a scheme for THz emission from the PQW resonantly coupled with the PC MM cavity and with the Fabry-Perot (FP) cavity. The device and its light emission are schematically shown in Fig. 5.1(a). The lasing of the PC MM cavity will enhance the ISB radiatvie transition accompanied with the surface emission of the terahertz EM wave; the lasing of the FP cavity will enhance the interband (IB) transition accompanied with the edge emission of the near-infrared (NIR) EM wave. We find the radiative ISB transition rate in the PQW can be enhanced by several orders of magnitude. Incorporating a compatible FP cavity will depopulate rapidly the electron and hole lowest subbands. Thus the ISB radiative process can surpass the ISB nonradiative process, allowing the THz emission power to be

higher than the heat generation power. The THz emission can easily achieve 10 W/cm^2.

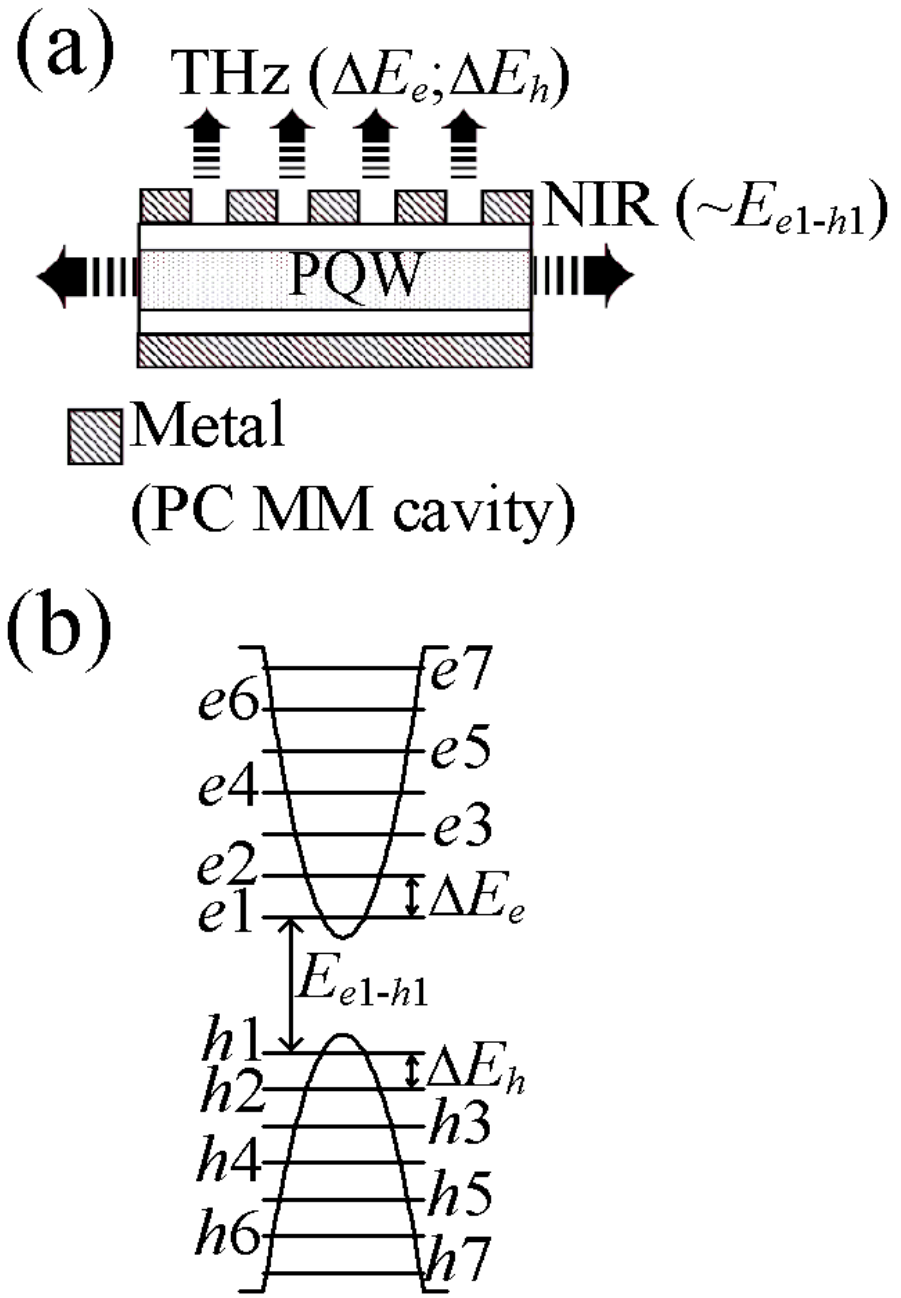

Fig. 5.1 (a) Schematic illustration of simultaneous interband and intersubband lasings from the PQWs coupled with the PC MM and FP cavities. (b) Illustrative PQWs with the levels of subband edges.

5.2 Description of Parabolic Quantum Wells

We consider, as a test case, a PQW structure of seven conduction and seven valence subbands as shown schematically in the Fig. 5.1(b). According to the order of the electron (hole) energies from low to high, the conduction (valence) subbands are denoted by $e1$ ($h1$), $e2$ ($h2$),…, $e7$ ($h7$). We assume that the conduction (valence) subband structures are parabolic with the same effective mass m_e (m_h). This is reasonable naturally for conduction subbands and also for valence subbands provided that a large strain makes negligible the coupling between the HH and the LH subbands in the energy region the holes mainly populate. For the case of $GaAs_{1-x}P_x$ PQW, this can be achieved as the PQW is pseudomorphically grown on the $Al_xGa_{1-x}As$ barrier layer. For the case of (001) biaxial strain, the LH subbands are raised so that the holes mainly populate the LH subbands.

In the present calculation, we use the parameters of $GaAs_{0.85}P_{0.15}$. The effective masses are given by linear interpolation between values of pure-GaAs and pure-GaP, and are set at $m_e=0.094m_0$ and $m_h=0.105m_0$. The m_h is the LH mass instead of the HH mass. The energy difference between the neighboring valence subbands is set at ΔE_h=4.1 meV, and thus that between the neighboring conduction subbands is given by $\Delta E_e=\Delta E_h(55m_h/45m_e)^{1/2}$=4.8 meV. Here the ratio 55:45 is the conduction-to-light-hole band offset ratio of the PQWs. It is obtained from the theory of [55] for the case that the strain caused by a thick $Al_xGa_{1-x}As$ (001) layer of the heterostructure is taken into account.

5.3 Photonic Crystal Metal-Metal Cavity

In the present calculation, we consider the case that the area of the PC MM cavity is so large that the PC MM modes can be treated as quasi-continuous with a 2D density of modes N. We do not consider a specific PC MM cavity structure but describe the PC MM cavity and its coupling with the PQW with two parameters. They are the quality factor Q and the spontane-

ous emission enhancement factor γ. The latter is defined as the ratio of the ISB spontaneous emission rates with and without the PC MM cavity being incorporated, and can be expressed as

$$\gamma = \frac{3\lambda}{2\lambda_c}\frac{N}{N_0}, \tag{5.1}$$

where N/N_0 is the Purcell factor, N_0 the 2D density of modes in the absence of the cavity, λ the wavelength of EM wave in the material, and λ_c an effective modal distance between the PC MM cavity and the PQW charactering the carrier-phonon coupling. It can be expressed as

$$\lambda_c = \frac{\int d\mathbf{r}\epsilon(\mathbf{r})\left|\mathbf{E}(\mathbf{r})\right|^2}{\epsilon_b \int d\mathbf{r}_{\|}\left|\mathbf{E}(\mathbf{r}_{\|}, z_0)\bullet\mathbf{e}_z\right|^2}, \tag{5.2}$$

where $\mathbf{E}$ is the electric field of the EM wave, ϵ the dielectric constant, ϵ_b the dielectric constant of the barrier, $\mathbf{e}_z$ is the unit vector perpendicular to the quantum well layer, and $z = z_0$ is at the center of the PQW. The detailed derivation of Eqs. (5.1) and (5.2) will be given in section 5.5. As can be seen, if the polarization of the PC MM cavity modes is in the plane of the quantum well, the λ_c is infinity, the PC MM cavity modes decouple from the PQW, γ=0, and hence the rate of spontaneous emission into the PC MM cavity modes is zero. One can obtain a high ISB radiative transition rate by designing a PC MM cavity with a short λ_c as well as a high Purcell factor N/N_0. The λ_c almost approaches to the thickness of the PC MM cavity L_{cav} when the metallic filling ratio of the PC approaches to unity (i.e., the PC becomes a metal plate) for the case of $\lambda \gg L_{cav}$. The PQW width should be the lower bound of L_{cav} and λ_c. In the present calculation, we set the Purcell factor N/N_0=1 and γ=10, so that the corresponding λ_c, for 1 THz EM wave given, by Eq. (5.1) is 13 μm. It is much larger than the thickness of the PQW (~100 nm). The quality factor is set at Q = 10 for all the PC MM modes of interest in the present calculation. It is smaller than that (Q~50) reported in [53]. The energy broadening of the PC MM cavity modes with energy in the vicinity of ΔE_σ is $\Gamma_\sigma = \Delta E_\sigma / Q$ (σ=e,h) and the corresponding lifetime is $\tau_{ph,\sigma} = \hbar/\Gamma_\sigma$. The photonic lifetime broadening for

the present case should be larger than the energy broadening due to the finite lifetime of the electronic states provided that the optical phonon process is not activated. Such electronic lifetime broadening should be smaller than the energy broadening observed in experiment (~0.15 meV at 20K) and hence considerably smaller than that in the present case (Γ_σ ~0.5 meV).

5.4 Rate Equations

The rate equations for carriers of the subbands under steady state can be written as

$$\sum_{i'=i}^{7}\left[R_{\sigma i'}+\left(1-\delta_{i,1}\right)\sum_{i''=1}^{i-1}R_{\sigma i'i''}\right]=\frac{J}{q},\quad \sigma=e,h;\ i=1,2,...,7 \tag{5.3}$$

where $R_{\sigma i'}$ is the annihilation rate of the carriers in subband i due to IB transition, $R_{\sigma ii'}$ the ISB transition rate for carrier transitions from subband σi to $\sigma i'$, and J the injection current density. The rates $R_{\sigma i}$ and $R_{\sigma ii'}$ are functions of carrier densities (denoted by $n_{\sigma i}$). The right-hand (left-) hand side of Eq. (5.3) is the sum of the generation (annihilation) rates of carriers in subbands higher than the subband σi. Here, we have assumed that only the highest subbands ($e7$ and $h7$) have a nonzero generation rate J/q. The fourteen equations in Eq. (5.3) only gives thirteen linear-independent equations because the equations for $(\sigma,i)=(e,1)$ and for $(\sigma,i)=(h,1)$ are linear dependent. This means that the annihilation rates for total electrons and for total holes are equal. Therefore, we require the charge neutrality condition,

$$\sum_{i=1}^{7}n_{ei}=\sum_{i=1}^{7}n_{hi}\,, \tag{5.4}$$

along with the rate equations to solve for the subband carrier densities. The ISB transition rate includes the radiative transition rate $R^{\mathrm{r}}_{\sigma ii'}$ and the nonradiative transition rate $R^{\mathrm{nr}}_{\sigma ii'}$. For PQW, the be approximately written as

$$R^{\mathrm{r}}_{\sigma ii'}=\frac{n_{\mathrm{ph},\sigma}}{\tau_{\sigma,i-1}}\left(n_{\sigma i}-n_{\sigma,i-1}\right)\delta_{i',i-1},\quad \sigma=e,h;\ i=2,3,...,6 \tag{5.5}$$

where $\tau_{\sigma i}$ is the lifetime of spontaneous emission into the PC MM cavity modes for $\sigma(i+1)\rightarrow\sigma i$ ISB transition of a single carrier (if other carriers were absent), $n_{\mathrm{ph},\sigma}$ the photon number of each excited PC MM mode with energy in the vicinity of ΔE_σ. Since the number of photons emitted by the PQW into the PC MM cavity modes is equal to that radiated out of the PC MM cavity under steady state, the photon number $n_{\mathrm{ph},\sigma}$ can be expressed as

$$n_{\mathrm{ph},\sigma} = \frac{\tau_{\mathrm{ph},\sigma}}{\Gamma_\sigma N\left(\Delta E_\sigma\right)} \sum_{i=2}^{7} R^r_{\sigma i,i-1} \,. \tag{5.6}$$

Here, we have supposed that only the PC MM cavity modes in the energy region between $\Delta E_\sigma - \Gamma_\sigma/2$ and $\Delta E_\sigma + \Gamma_\sigma/2$ are excited by the PQW, and they are excited equally so that each mode in the energy region between $\Delta E_\sigma - \Gamma_\sigma/2$ and $\Delta E_\sigma + \Gamma_\sigma/2$ has the same photon number $n_{\mathrm{ph},\sigma}$. We approximate the nonradiative transition rate $R^{\mathrm{nr}}_{\sigma ii'}$ as

$$R^{\mathrm{nr}}_{\sigma ii'} = r_{\sigma ii'}\left[n_{\sigma i} - x\Theta(x)\right], \quad i > i' \tag{5.7}$$
$$x = n_{\sigma i'} - (i - i')\delta n_\sigma$$

where δn_σ is the number of states of a single subband of type σ in the energy interval ΔE_σ and $\Theta(x)$ the unit step function (i.e., $\Theta(x)=1$ if $x\geq 0$, $\Theta(x)=0$ if $x<0$). The $r_{\sigma ii'}$ is the rate of the nonradiative ISB transition of a single carrier from the subband edge of σi to the subband $\sigma i'$ if other carriers were absent. It includes the acoustic deformation potential (ADP) scattering rate $r^{\mathrm{ADP}}_{\sigma ii'}$ and the piezoelectric (PZ) scattering rate $r^{\mathrm{PZ}}_{\sigma ii'}$. In general, $r^{\mathrm{ADP}}_{\sigma ii'}$ and $r^{\mathrm{PZ}}_{\sigma ii'}$ are comparable at low temperature. The general form of $r^{\mathrm{ADP}}_{\sigma ii'}$ has been derived in [56], and that of $r^{\mathrm{PZ}}_{\sigma ii'}$ can be derived in a similar way. In the present calculation, they can be written as

$$r_{\sigma ii'}^{\mathrm{ADP}} = \frac{D_\sigma^2 m_\sigma^2 \Delta E_\sigma}{2\pi\hbar^4 \rho v_s}\left(2N_{\sigma,i-i'}+1\right)\int_0^\infty dy\left(G_{ii'}(y)\right)^2\sqrt{2(i-i')+y^2}$$

$$r_{\sigma ii'}^{\mathrm{PZ}} = \left(\frac{qe_{\mathrm{PZ}}}{\epsilon}\right)^2 \frac{2m_\sigma}{\rho v_s \hbar^2}\left(2N_{\sigma,i-i'}+1\right)\int_0^\infty dy \frac{\left(G_{ii'}(y)\right)^2}{\sqrt{2(i-i')+y^2}} \tag{5.8}$$

$$G_{ii'}(y) = \frac{1}{\sqrt{2^{i+i'}\pi i!\,i'!}}\int_{-\infty}^{\infty} d\xi e^{-\xi^2} H_i(\xi) H_{i'}(\xi)\exp(-iy\xi)$$

where D_σ is the hydrostatic deformation potential constant (HDPC), ρ the material density, v_s the sound velocity, e_{PZ} the piezoelectric constant, and H_i the Hermite polynomial of degree i. The $N_{\sigma,i\text{-}i'}$ is the number of phonons participating in the carrier-phonon scattering leading to the ISB transition between σi and $\sigma i'$, and can be written as

$$N_{\sigma,i-i'} = \frac{1}{\exp\left(\dfrac{m_\sigma v_s^2 + v_s\sqrt{\left(m_\sigma v_s\right)^2 + 2m_\sigma \Delta E_\sigma (i-i')}}{k_{\mathrm{B}}T}\right)-1}, \tag{5.9}$$

where k_{B} is the Boltzmann constant. In general, the intrasubband scattering rate is about one order in magnitude larger than the ISB scattering rate. Provided that the intrasubband phonon scattering rate is set at infinity, the carriers in each subband are in equilibrium with the lattice which has a low temperature (4.22K). This may result in a considerable overestimate of the heat generation. In deriving Eq. (5.7), and only for this equation, we set the carrier temperature of each subband at 0K for simplicity. Although the intrasubband equilibrium is assumed, the ISB equilibrium is not necessarily established.

The IB recombination rate $R_{\sigma i}$ can be written as $R_{ei} = \sum_{i'} R_{ei\text{-}hi'}$ and $R_{hi} = \sum_{i'} R_{ei'\text{-}hi}$ where $R_{ei\text{-}hi'}$ is the recombination rate between subbands e_i and $h_{i'}$. We approximate $R_{ei\text{-}hi'}$ by

$$R_{ei\text{-}hi'} = \frac{2}{\tau_{ei\text{-}hi'}}\frac{m_e m_h}{\left(m_e+m_h\right)^2}\left(f_{hi'}n_{ei} + f_{ei}n_{hi'}\right), \tag{5.10}$$

where $f_{\sigma i}$ is the carrier population probability at the edge of subband σi which is in equilibrium with the lattice (T=4.22 K), $\tau_{ei\text{-}hi'}$ the life time for IB transition of an electron from the

edge of subband *ei* to that of *hi'* if the latter were empty of electrons. It can be written as

$$\tau_{ei-hi'}^{-1} = \frac{5q^2\epsilon^{1/2}E_P E_{ei-hi'}}{48\pi\epsilon_0 m_0 \hbar^2 c^3}\left|\int_{-\infty}^{\infty} dz g_{ei}(z)\, g_{hi'}(z)\right|^2 \tag{5.11}$$

where $g_{\sigma i}$ (z) is the *z*-dependent envelope function of subband σi, $E_{ei\text{-}hi'}$ the energy separation between the edges of subbands *ei* and *hi'*, E_P the energy equivalent of the IB momentum matrix element [57], and *c* the speed of light in vacuum. In deriving Eq. (5.11), we suppose that the cavity modes have electric fields with $|\mathbf{e}_z \bullet \mathbf{E}| = |\mathbf{e}_z \times \mathbf{E}|$ in the PQW.

As mentioned earlier, we use the parameter of $GaAs_{0.85}P_{0.15}$. The dielectric constant ϵ is set at 12.6. The other parameters in the rate equations are given by linear interpolation between the values of pure-GaAs and pure-GaP. Therefore, we obtain the parameter E_P=25.2 eV, the material density ρ=5139 kg/cm^3, the sound velocity v_s =5324 m/s, the piezoelectric constant e_{PZ} =0.15 C/m^2, and HDPC D_e=7.17 eV and D_h=1.24 eV.

5.5 Intersubband Radative Transition Rates

In this section, we will investigate the effect of the cavity modes on the ISB spontaneous emission rate, and derive the enhancement factor γ given by Eqs. (5.1) and (5.2). As mentioned earlier, γ is defined as the ISB spontaneous emission rate in the presence of the PC MM cavity normalized by that in the absence of the PC MM cavity. Therefore, we will begin with the case in the absence of the PC MM cavity. According to Fermi's golden rule, the rate of ISB transition between the subband states $|i\mathbf{k}_i\rangle$ and $|j\mathbf{k}_j\rangle$ can be written as

$$\frac{1}{\tau_{i\mathbf{k}_i j\mathbf{k}_j}} = \frac{2\pi E_{sp}^2}{\hbar}\sum_{\mathbf{k}\alpha}\delta\left(\left|E_i(\mathbf{k}_i) - E_j(\mathbf{k}_j)\right| - \frac{\hbar c k}{\sqrt{\epsilon_b}}\right)\left|\langle i\mathbf{k}_i|\, q\mathbf{r}\bullet\mathbf{e}_{\mathbf{k}\alpha}\,|j\mathbf{k}_j\rangle\right|^2, \tag{5.12}$$

where $\mathbf{e}_{\mathbf{k}\alpha}$ is the unit polarization vector of the EM wave with wave vector $\mathbf{k}$ and polarization α, $E_i(\mathbf{k}_i)$ the energy of the *i*th subbnand states with wave vector $\mathbf{k}_i$, E_{sp} the magnitude of electric field of a plane wave with a single photon within a unit volume. The E_{sp} satisfies

$$2\int d\mathbf{r}\epsilon(\mathbf{r})\left|E_{\mathrm{sp}}(\hbar\omega)\right|^2 = \hbar\omega;\ \hbar\omega = \left|E_i(\mathbf{k}_i) - E_j(\mathbf{k}_j)\right|. \tag{5.13}$$

The **r**-dependent dielectric constant $\epsilon(\mathbf{r})$ can be approximated by ϵ_{b}, because the EM wave is extended and the PQW is much thinner than the barrier so that most of the EM wave distribute in the barrier. Another reason is that the dielectric constants of the PQW and of the barrier are in general nearly equal. The selection rule causes that only the *z*-component of the dipole matrix element is not vanished. Furthermore, neglecting the momentum of the photon, we can express the electric dipole matrix element as $\langle i\mathbf{k}_i | q\mathbf{r} | j\mathbf{k}_j \rangle = d_{ij}\delta_{\mathbf{k}_i,\mathbf{k}_j}\mathbf{e}_z$. Therefore, we can rewrite Eq. (5.12) as

$$\frac{1}{\tau_{i\mathbf{k}_i j\mathbf{k}_j}} = \frac{2\pi}{\hbar}\frac{E_{ij}}{2\epsilon_{\mathrm{b}}}\left|d_{ij}\right|^2 \delta_{\mathbf{k}_i,\mathbf{k}_j}\sum_{\mathbf{k}\alpha}\delta\left(E_{ij} - \frac{\hbar ck}{\sqrt{\epsilon_{\mathrm{b}}}}\right)\left|\mathbf{e}_z \bullet \mathbf{e}_{\mathbf{k}\alpha}\right|^2, \tag{5.14}$$

where, E_{ij} is the energy difference between subbands *i* and *j*. The sum in Eq. (5.14) is just one third of the 3D density of modes for the bulk material (denoted by N_{b}). Therefore,

$$\frac{1}{\tau_{i\mathbf{k}_i j\mathbf{k}_j}} = \frac{1}{3}\frac{\pi E_{ij}}{\hbar\epsilon_{\mathrm{b}}}\left|d_{ij}\right|^2 \delta_{\mathbf{k}_i,\mathbf{k}_j} N_{\mathrm{b}}(E_{ij}), \tag{5.15}$$

The spontaneous emission rate in the absence of PC MM cavity is obtained by summing over all the final states

$$\frac{1}{\tau_{0,ij}} = \sum_{\mathbf{k}_j}\frac{1}{\tau_{i\mathbf{k}_i j\mathbf{k}_j}} = \frac{1}{3}\frac{\pi E_{ij}}{\hbar\epsilon_{\mathrm{b}}}\left|d_{ij}\right|^2 N_{\mathrm{b}}(E_{ij}). \tag{5.16}$$

As can be seen, it is not a function of the wave vector of the initial state. Equation (5.16) can also be written as

$$\frac{1}{\tau_{0,ij}} = \frac{1}{3}\frac{E_{ij}^3\sqrt{\epsilon_{\mathrm{b}}}}{\pi\hbar^4 c^3}\left|d_{ij}\right|^2 \tag{5.17}$$

Having obtained the ISB radiative transition rate in the absence of PC MM cavity, we go on to derive that in the presence of the PC MM cavity. Similarly, we begin with Fermi's gol-

den rule. The rate of the ISB transition between the states $|i\mathbf{k}_i\rangle$ and $|j\mathbf{k}_j\rangle$ can be written as

$$\frac{1}{\tau_{i\mathbf{k}_i j\mathbf{k}_j}} = \frac{2\pi}{\hbar}\sum_{\mathbf{k}_{\|}\alpha}\delta\left(\left|E_i(\mathbf{k}_i) - E_j(\mathbf{k}_j)\right| - \hbar\omega_{\mathrm{PC}}(\mathbf{k}_{\|}\alpha)\right)\left|\langle j\mathbf{k}_j|q\mathbf{r}\bullet\mathbf{E}_{\mathbf{k}_{\|}\alpha}|i\mathbf{k}_i\rangle\right|^2 \qquad (5.18)$$

where $\omega_{\mathrm{PC}}(\mathbf{k}_{\|}\alpha)$ is the dispersion relation and $\mathbf{E}_{\mathbf{k}_{\|}\alpha}$ the electric field caused by a single photon within a unit area for the PC MM cavity mode with the wave vector $\mathbf{k}_{\|}$ and the polarization α. Here, the index α can be generalized to include other good quantum numbers (if exists) of the PC MM cavity modes. The expression of Eq. (5.18) is useful if $\omega_{\mathrm{PC}}(\mathbf{k}_{\|}\alpha)$ and $\mathbf{E}_{\mathbf{k}_{\|}\alpha}$ were known. However, as mentioned earlier, we do not intend to consider any specific PC MM cavity structure and hence any specific $\omega_{\mathrm{PC}}(\mathbf{k}_{\|}\alpha)$ and $\mathbf{E}_{\mathbf{k}_{\|}\alpha}$. Therefore, we rewritten Eq. (5.18) as

$$\frac{1}{\tau_{i\mathbf{k}_i j\mathbf{k}_j}} = \frac{2\pi}{\hbar}N\left(\left|E_i(\mathbf{k}_i) - E_j(\mathbf{k}_j)\right|\right)\left|\langle j\mathbf{k}_j|q\mathbf{r}\bullet\mathbf{E}(\mathbf{r})|i\mathbf{k}_i\rangle\right|^2. \qquad (5.19)$$

Here the selection rule of momentum (i.e., $\langle j\mathbf{k}_j|q\mathbf{r}\bullet\mathbf{E}(\mathbf{r})|i\mathbf{k}_i\rangle \propto \delta_{\mathbf{k}_i,\mathbf{k}_j}$) is no longer strictly valid because the photons can gain momenta through the scattering by the PC; the ISB transitions between states of different wave vectors are allowed through emitting photons into the PC MM cavity modes. However, the matrix element $\langle j\mathbf{k}_j|q\mathbf{r}\bullet\mathbf{E}(\mathbf{r})|i\mathbf{k}_i\rangle$ has a significant value only when $|\mathbf{k}_j - \mathbf{k}_i| \lesssim 2\pi/a_{\mathrm{PC}}$, where a_{PC} is the lattice constant of the PC. Therefore, the density of modes of Eq. (5.19) can be approximated by $N(E_{ij})$ for the case that a_{PC} is much larger than the lattice constant of the material. In this case, the electric field **E**(**r**) should be slowly varying over a unit cell. Therefore, the electric dipole matrix element can be written as

$$\left\langle j\mathbf{k}_j \left| q\mathbf{r}\bullet\mathbf{E}(\mathbf{r}) \right| i\mathbf{k}_i \right\rangle = q\int d\mathbf{r} F^*_{j\mathbf{k}_j}(\mathbf{r}) F_{i\mathbf{k}_i}(\mathbf{r}) \mathbf{E}(\mathbf{r})\bullet\mathbf{r} d\mathbf{r}\,, \tag{5.20}$$

where $F_{i\mathbf{k}}(\mathbf{r})$ is the envelope function of the subband state $|i\mathbf{k}\rangle$. It can be expressed as

$$F_{i\mathbf{k}}(\mathbf{r}) = \exp\left(i\mathbf{k}\bullet\mathbf{r}_{\|}\right) g_i(z) \tag{5.21}$$

In general, the thickness of the PQW is so small that the electric field in the PQW can be approximated by $\mathbf{E}(\mathbf{r}_{\|}, z_0)$. Therefore, the matrix element can be written as

$$\left\langle j\mathbf{k}_j \left| q\mathbf{r}\bullet\mathbf{E}(\mathbf{r}) \right| i\mathbf{k}_i \right\rangle = d_{ij}\int e^{i\left(\mathbf{k}_i-\mathbf{k}_j\right)\bullet\mathbf{r}_{\|}} \mathbf{E}(\mathbf{r}_{\|}, z_0)\bullet\mathbf{e}_z d\mathbf{r}_{\|}\,. \tag{5.22}$$

In deriving Eq. (5.22) we have used the orthogonality of the functions $g_i(z)$. The (5.19) can be written as

$$\frac{1}{\tau_{i\mathbf{k}_i j\mathbf{k}_j}} = \frac{2\pi\left|d_{ij}\right|^2}{\hbar} N(E_{ij}) \left| \int e^{i\left(\mathbf{k}_i-\mathbf{k}_j\right)\bullet\mathbf{r}_{\|}} \mathbf{E}(\mathbf{r}_{\|}, z_0)\bullet\mathbf{e}_z d\mathbf{r}_{\|} \right|^2 \tag{5.23}$$

For the electron initially at subband state $|i\mathbf{k}_i\rangle$, the rate of the spontaneous emission for the ISB transition to the subband j is $\tau_{ij}^{-1}(\mathbf{k}_i) = \sum_{\mathbf{k}} \tau^{-1}_{i\mathbf{k}_i j\mathbf{k}}$. In fact, similar to $\tau_{0,ij}^{-1}$, τ_{ij}^{-1} is not a function of the wave vector of the initial state. It can be written as

$$\frac{1}{\tau_{ij}} = \frac{2\pi\left|d_{ij}\right|^2}{\hbar} N(E_{ij}) \int d\mathbf{r}_{\|} \left| \mathbf{E}(\mathbf{r}_{\|}, z_0)\bullet\mathbf{e}_z \right|^2, \tag{5.24}$$

or

$$\frac{1}{\tau_{ij}} = \frac{2\pi\left|d_{ij}\right|^2}{\hbar} N(E_{ij}) \frac{\int dz \int d\mathbf{r}_{\|} \epsilon(\mathbf{r}) \left|\mathbf{E}(\mathbf{r})\right|^2}{\epsilon_{\mathrm{b}}\lambda_{\mathrm{c}}} \tag{5.25}$$

Since $\mathbf{E}(\mathbf{r})$ is the electric field caused by a single photon, it satisfies

$$2\int dz \int d\mathbf{r}_{\|} \epsilon(\mathbf{r}) \left|\mathbf{E}(\mathbf{r}_{\|}, z)\right|^2 = E_{ij}\,. \tag{5.26}$$

Substituting Eq. (5.26) into Eq. (5.25), we obtain

$$\frac{1}{\tau_{ij}} = \frac{\pi \left| d_{ij} \right|^2 E_{ij}}{\hbar \epsilon_b \lambda_c} N\left(E_{ij}\right). \tag{5.27}$$

According to the definition of the spontaneous emission enhancement factor γ, it is $\gamma = \tau_{0,ij} / \tau_{ij}$. From Eqs. (5.16) and (5.27), γ can be written as

$$\gamma = \frac{3}{\lambda_c} \frac{N\left(E_{ij}\right)}{N_b\left(E_{ij}\right)} \tag{5.28}$$

The 3D density of modes N_b can be expressed in terms of the 2D density of modes N_0,

$$N_b\left(E_{ij}\right) = \frac{2}{\lambda} N_0\left(E_{ij}\right). \tag{5.29}$$

Therefore, we obtain the final expression of the spontaneous emission enhancement factor γ,

$$\gamma = \frac{3\lambda}{2\lambda_c} \frac{N}{N_0} \tag{5.30}$$

Chapter 6

Results and Discussion

6.1 Effects of the PC MM Cavity

In the absence of a PC MM cavity, only the edge emission of the THz EM wave is available because the radiative ISB transition is forbidden for the EM wave polarized along the *z* direction. Furthermore, almost all the energy of carriers, as mentioned earlier, is dissipated through the nonradiative ISB transition and is converted into heat because the nonradiative transition rate is much larger than the radiative transition rate. Fig. 6.1 shows the carrier-phonon scattering rate of a single carrier (i.e., $r_{\sigma i}^{\mathrm{ADP}} = \sum_{i'=1}^{i-1} r_{\sigma ii'}^{\mathrm{ADP}}$, $r_{\sigma i}^{\mathrm{PZ}} = \sum_{i'=1}^{i-1} r_{\sigma ii'}^{\mathrm{PZ}}$) as function of the subband index *i* of the subband which the carrier populates. The subscript e (h) denotes the electron-phonon (hole-phonon) scattering. As can be seen, the carrier-phonon scattering rate is of the order of 10^9~10^{10} s^{-1} which is about 10^5 times higher than the spontaneous emission rate (about 10^4~10^5 s^{-1}).

Two other features of the carrier-phonon scattering can be seen from Fig. 6.1. The first is that the $\mathrm{ADP_e}$ scattering rate is much higher than the $\mathrm{ADP_h}$ scattering rate. This is because the ADP scattering rate is proportional to the square of the HDPC, and there is a large difference in the magnitude of HDPC between the valence band and the conduction band. The second is that the subband index (*i*) dependence of the $r_{\sigma i}^{\mathrm{ADP}}$ is qualitative different from that of the $r_{\sigma i}^{\mathrm{PZ}}$. The $r_{\sigma i}^{\mathrm{ADP}}$ almost increases linearly with the index *i* because the $r_{\sigma ii'}^{\mathrm{ADP}}$ is almost a constant for different final states σi'. However, the $r_{\sigma i}^{\mathrm{PZ}}$ increases with the subband index *i* and then saturates to a constant because the $r_{\sigma ii'}^{\mathrm{PZ}}$ is smaller for a smaller *i*'. This is due to the intrinsic properties of electrostatic interaction that the faster moving carriers scatter less than the

slower moving carriers [58]. For the smaller index *i*' (i.e., the larger *i*–*i*'), the final state of ISB transition $\sigma i \to \sigma i'$ can gain a higher kinetic energy.

The presence of the PC MM cavity can introduce a 2D density of mode of the PC MM cavity. The *z* component of the polarization of the PC MM cavity mode can be considerable in the PQW so that the carrier-photon coupling is significant and the surface emission is available. Figure 6.2(a) shows the modal photon number $n_{\mathrm{ph},\sigma}$ and the THz emission power $W_{\mathrm{ph},\sigma}$ (σ=*e*,*h*) as functions of the injection current *J*. As can be seen, $n_{\mathrm{ph},\sigma}$ increases with *J* and the ISB stimulated emission rate, which is $n_{\mathrm{ph},\sigma}$ times the spontaneous emission rate, can increase by several orders of magnitude. Therefore, the radiative ISB transition rate is comparable to the nonradiative ISB transition rate, and hence the output of the THz emission is almost comparable to the heat. This can be seen from Fig. 6.3 (a), which shows the *J* dependence of the heat generation. In addition, Fig. 6.3 (a) shows the *J* dependence of the carrier density n_{tot}, which is defined as the total 2D carrier density divided by the PQW width. We find the carrier density n_{tot} is almost proportional to the heat generation. In other words, the average carrier -phonon scattering rate is almost constant with increasing *J* (and hence n_{tot}).

When *J* is further increased beyond a critical value J_c, the separation of the quasi-Fermi level of subband *e*7 from the edge of subband *e*1 can be larger than the optical phonon energy $\hbar\omega_{\mathrm{op}}$ (~36 meV) to activate optical phonon emission. This will degrade seriously device performance, such as increasing the threshold current, generating more heat, and hence lowering the ISB quantum efficiency (QE). For the present calculation, J_c is about 382 A/cm^2 below which the THz emission power is lower than 2 A/cm^2.

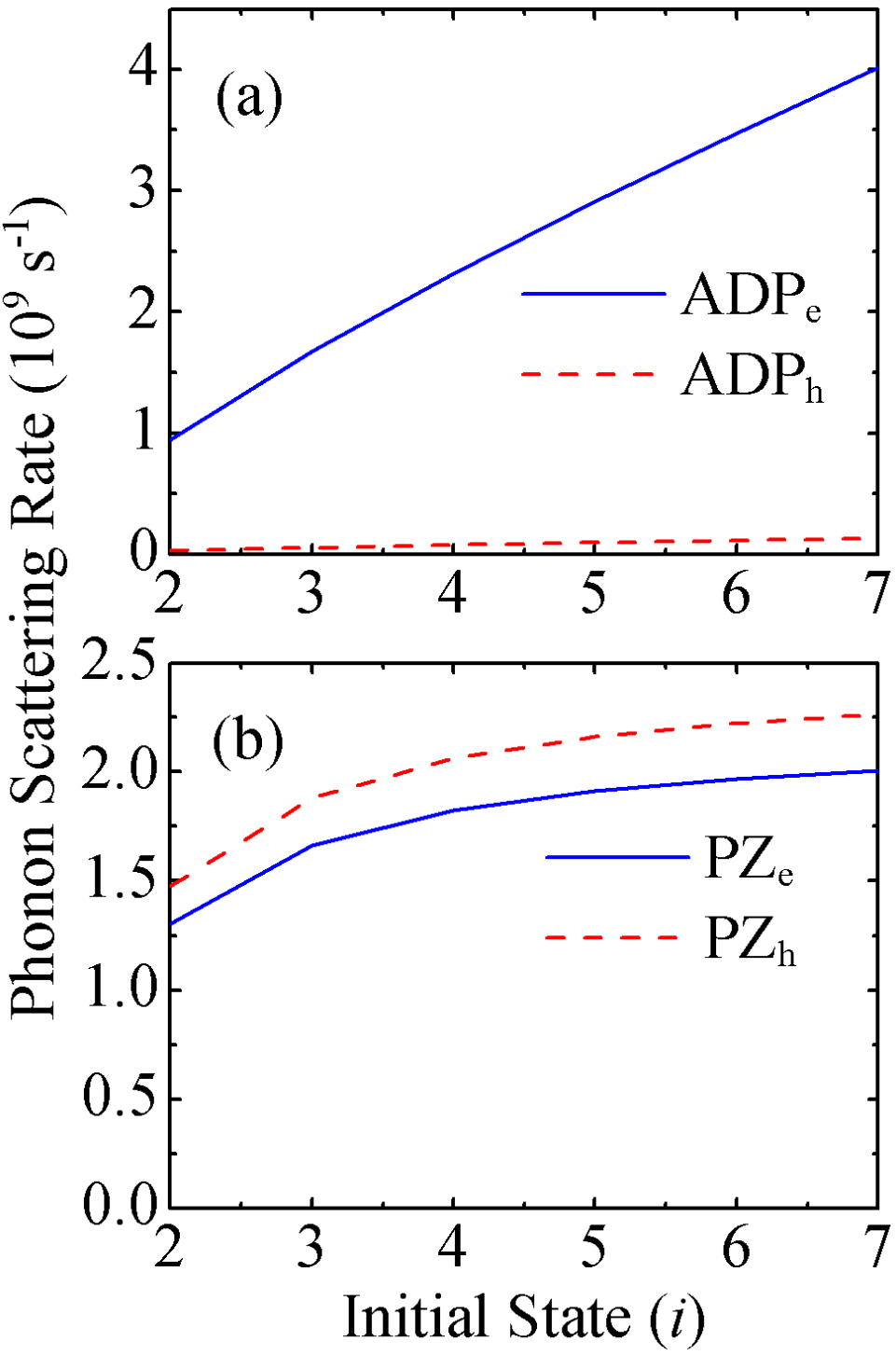

Fig. 6.1 The rates of different carrier-phonon scattering mechanisms for a single electron (hole) at the conduction (valence) subband *ei* (*hi*).

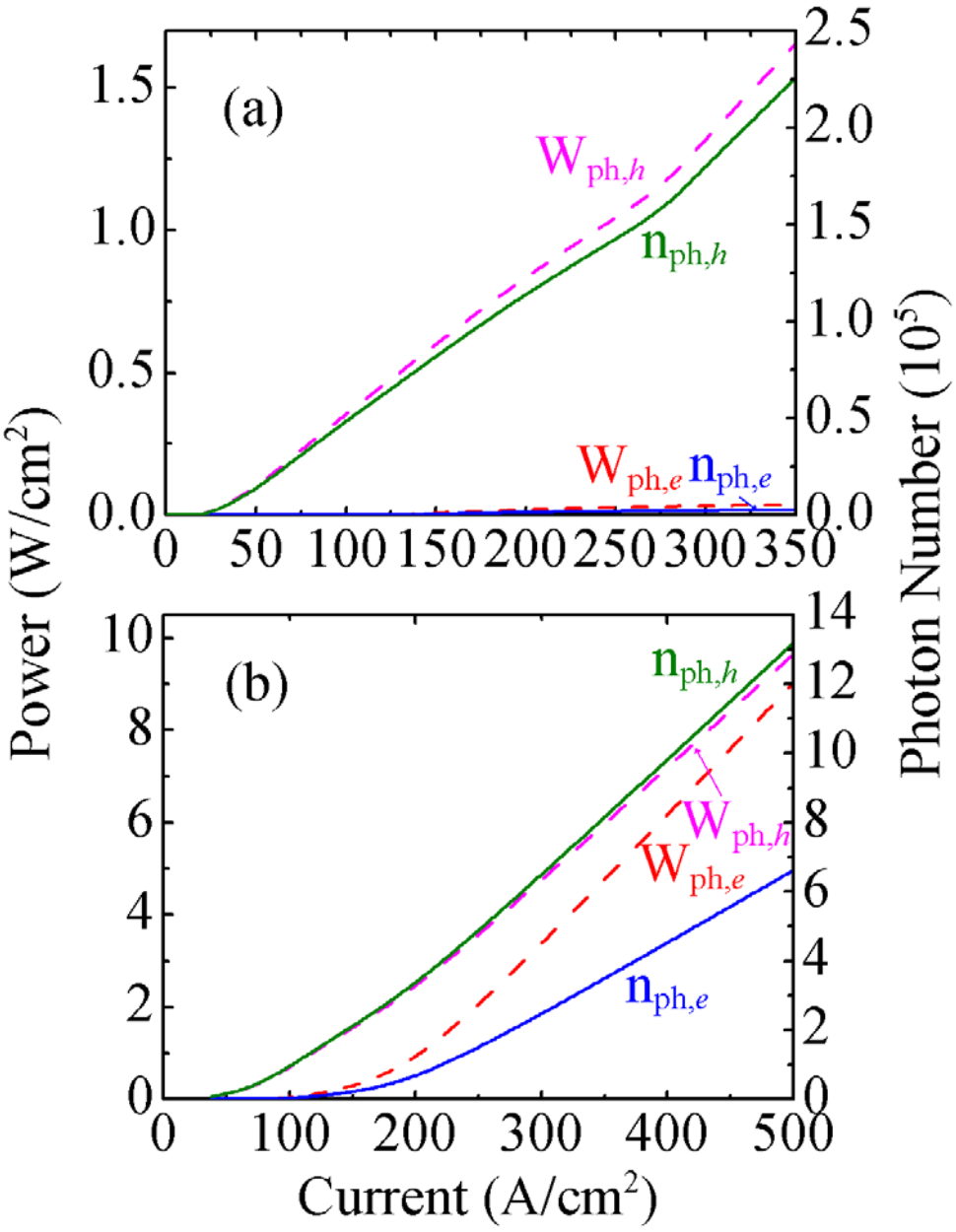

Fig. 6.2 The photon number $n_{ph,\sigma}$ of PC MM cavity modes and the THz emission power $W_{ph,\sigma}$ (σ=e,h) versus the injection current J for (a) without and (b) with the FP cavity.

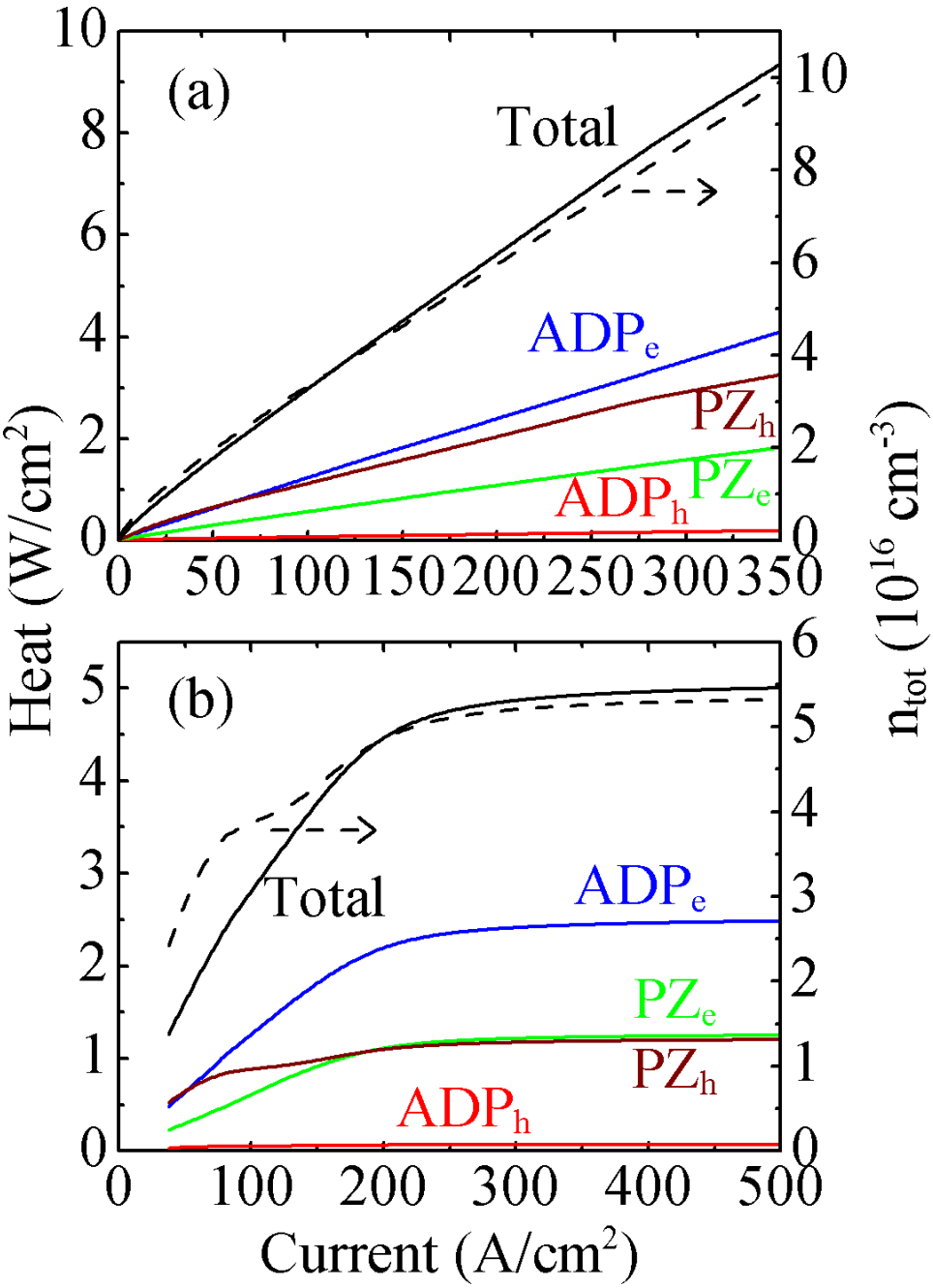

Fig. 6.3 The carrier density n_{tot}, the total heat power, and the contributions of different scattering mechanisms to the heat generation as functions of the injection current J for (a) without and (b) with the FP cavity.

6.2 Effects of the Heterogeneous Cavities

The ISB QE can be significantly improved by introducing a FP cavity. To gain an insight, we show in Fig. 6.4 the IB gains g_i at seven photon energies $\hbar\omega = E_{ei-hi}$ (i=1,2,...,7) versus J for (a) without and (b) with a FP cavity. The gain spectrum has local maxima at $\hbar\omega = E_{ei-hi}$ if the scattering broadenings are small [59]. Without the FP cavity, g_1 increases rapidly with J and then saturates at a value g_{s1} when f_{e1} and f_{h1} approach unity. Differently, the gains g_i (i≥2) increase from more negative values, because the absorption increases with the photon energy in the absence of excitation, and then saturate at much higher currents. Therefore, the lasing photon energy is between $E_{e1\text{-}h1}$ and $E_{e2\text{-}h2}$ if there is a FP cavity with a threshold gain $g_{th}<g_{s1}$. Once IB lasing, the gain g_1 is pinned at g_{th}, as Fig. 6.4(b) shows. The lasing depopulates rapidly subbands $e1$ and $h1$, and hence establishes ISB population inversion. This may lead to ISB lasing of the PC MM cavity modes. The ISB lasing further enhances ISB transitions, by stimulated emission, of carriers in all subbands except the lowest ones. As a result, all the subband carrier densities are finally suppressed at fixed values, almost independent of J. This is reflected by the negative gains g_i (i≥2) in Fig. 6.4(b) as the current density J is higher than 100 A/cm^2. Here we set g_{th} =350 cm^{-1} for the lasing mode with energy $\hbar\omega = E_{e1-h1}$. Benefits of the carrier density suppression are threefold. The first is that the $e1 \rightarrow h1$ IB lasing remains steady no matter how high the current is. This ensures the stability of THz ISB lasing. The second is that optical phonon scattering is prohibited. At deep lasing, the separation of the quasi-Fermi level of subband $e7$ from the lowest subband edge is smaller than the optical phonon energy by about 4.7 meV. The third is that acoustic phonon scattering and the heat generation are suppressed. Fig. 6.3 (b) shows the heat power and the carrier density n_{tot} as functions of J in the presence of the FP cavity. As can be seen, the heat as well as n_{tot} saturates, as ISB lasing. The heat is much smaller than that without the FP cavity at high J. In the

saturation region, any increase in J does not cause heat generation but totally contributes THz emission, and hence the ISB process is dominated by the radiative process. The heat deviates from the linear dependence on n_{tot} in the region around J~100 A/cm^2 because the region is a transition region between nonradiative-process-dominated (NPD) and radiative-process-dominated (RPD) cases. With the increase of J (and hence n_{tot}), the carriers tend to populate higher subbands, which have higher nonradiative scattering rates $r_{\sigma i}^{ADP}$ and $r_{\sigma i}^{PZ}$. Therefore, the slope of heat versus n_{tot} for the RPD case is higher than that for the NPD case, and varies markedly with J (and hence n_{tot}) in the transition region. With the FP cavity, the threshold of ISB lasing is reduced. Above threshold, the THz emission power $W_{ph,\sigma}$ and the modal photon number $n_{ph,\sigma}$ increase linearly with J, as shown in Fig. 6.2(b), and the emission has a slope efficiency almost equal to $6\Delta E_\sigma / q$. This indicates that, besides those for the fixed heat generation rate, additional ISB transitions proceed by emitting THz photons. The factor 6 arises from there being 6 equally energy spacings of the subbands for each PQW. The more subbands the PQW has, the higher the slope efficiency will be, but the activation of optical phonon scattering sets its upper bound at $\hbar\omega_{op} / q$. At high J, the electron ISB lasing has a higher emission power than the hole lasing because the former has a higher slope efficiency.

In the present calculation, we do not take account of the ISB carrier-carrier (CC) scattering. The ISB CC scattering can dominate the ISB process for high carrier density. However, it should not be important in our case because the carrier density can remain low (<5.5×10^{16} cm^{-3}) with the scheme of PQW resonantly coupled with a PC MM cavity and a FP cavity [Fig. 4(b)]. The carrier density at lasing can be further reduced by optimizing the cavities, such as enhancing Q and γ (through enhancing the Purcell factor and reducing the characteristic length λ_c) and lowering the threshold gain g_{th} of the FP cavity modes. Figure 6.5 shows the carrier density n_{tot} versus J for different γ and g_{th}. We can find that the reduction in n_{tot} is

prominent when γ is enhanced and/or g_{th} is lowered. Therefore, the emission efficiency can be further improved and the heat generation can be further alleviated.

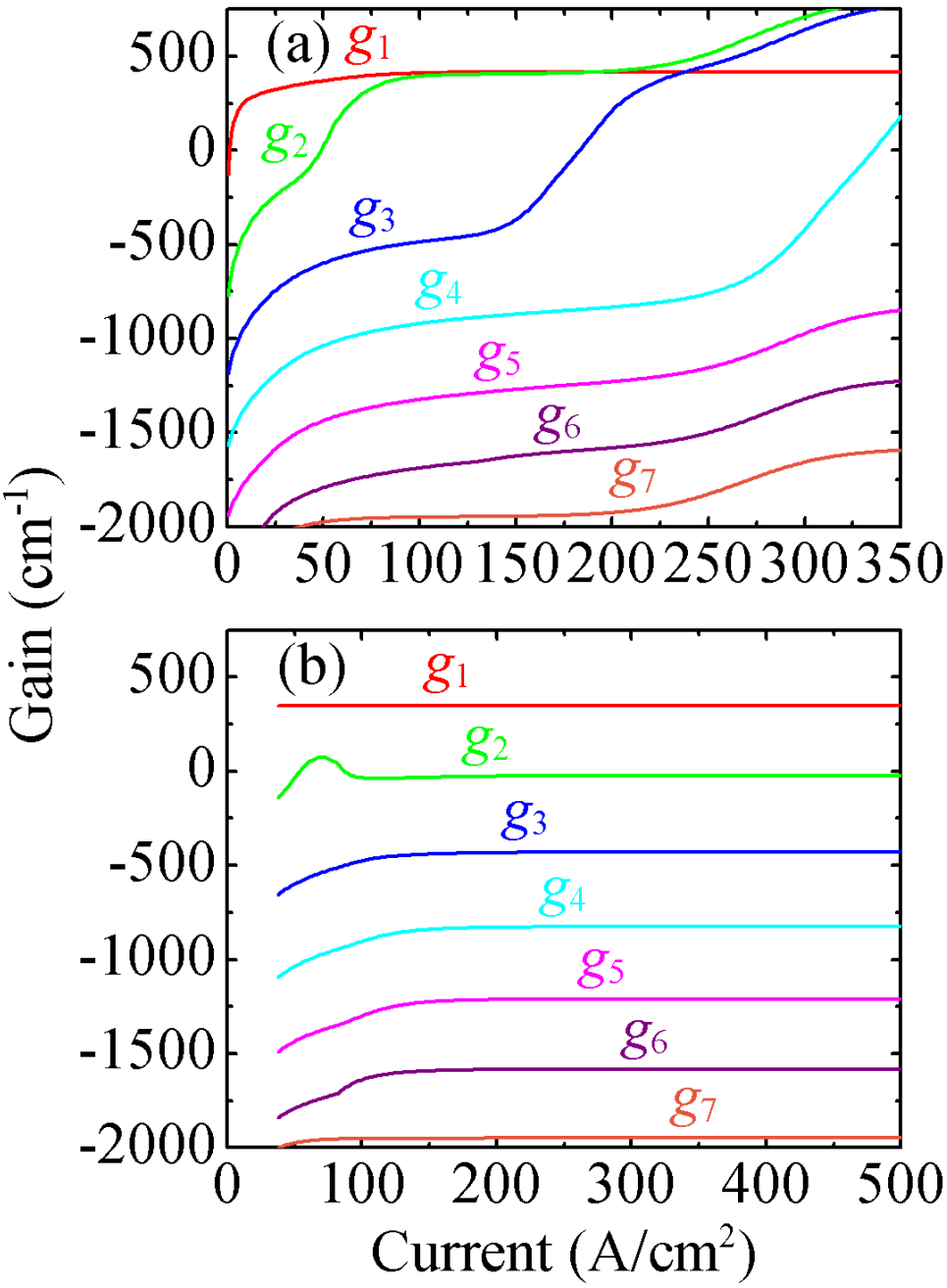

Fig. 6.4 The interband gains g_i at photon energies $E_{ei\text{-}hi}$ (i=1,2,…,7) versus the injection current J for (a) without and (b) with the FP cavity.

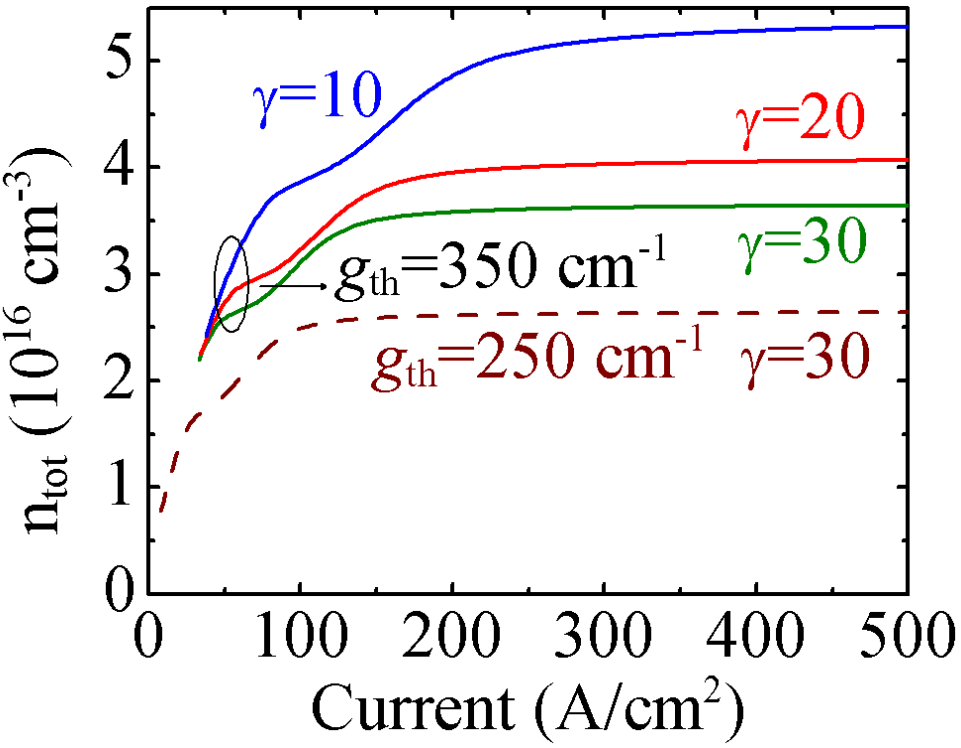

Fig. 6.5 The carrier density n_{tot} versus the injection current J for different threshold gains g_{th} of the FP modes and different intersubband spontaneous emission enhancement factors γ.

6.3 Summary

In summary, we have proposed a scheme for THz emission. In this scheme, the PQWs are resonant coupled with PC MM and FP cavities. The in-resonance PC MM cavity can increase the ISB radiative transition rate by several orders; the in-resonance FP cavity can depopulate the carriers through the IB lasing so that not only the optical phonon scattering is prohibited but also the acoustic phonon scattering is suppressed. When ISB and IB lasings occur simultaneously, the emission power increases linearly with current while the heat generation is almost constant. In this case, the slope efficiency of emission power is nearly equal to that without the phonon scattering.

References

[1] B. Ferguson, X.C. Zhang, "Materials for terahertz science and technology," Nat Mater, **1**, 26-33 (2002).

[2] P.H. Siegel, "Terahertz technology," Ieee T Microw Theory, **50**, 910-928 (2002).

[3] P.H. Siegel, "Terahertz technology in biology and medicine," Ieee T Microw Theory, **52**, 2438-2447 (2004).

[4] K. Sakai, Terahertz Optoelectronics, Springer, Berlin, 2005.

[5] M. Tonouchi, "Cutting-edge terahertz technology," Nat Photonics, **1**, 97-105 (2007).

[6] Y.S. Lee, Principles of terahertz science and technology, Springer, Boston, 2009.

[7] X.-C. Zhang, J. Xu, Introduction to THz wave photonics, Springer, New York, 2010.

[8] B.S. Williams, "Terahertz quantum-cascade lasers," Nat Photonics, **1**, 517-525 (2007).

[9] Y.P. Gousev, I.V. Altukhov, K.A. Korolev, V.P. Sinis, M.S. Kagan, E.E. Haller, M.A. Odnoblyudov, I.N. Yassievich, K.A. Chao, "Widely tunable continuous-wave THz laser," Appl. Phys. Lett., **75**, 757-759 (1999).

[10] A.K. Ramdas, S. Rodriguez, "Spectroscopy of the solid-state analogues of the hydrogen atom: donors and acceptors in semiconductors," Rep. Prog. Phys., **44**, 1297-1387 (1981).

[11] S.T. Pantelides, "The electronic structure of impurities and other point defects in semiconductors," Rev. Mod. Phys., **50**, 797 (1978).

[12] R.L. Jones, P. Fisher, "Excitation spectra of group III impurities in germanium," J. Phys. Chem. Solids, **26**, 1125-1131 (1965).

[13] H.P. Soepangkat, P. Fisher, "Transverse Zeeman Effect of the Excitation Spectra of Boron and Thallium Impurities in Germanium," Phys. Rev. B, **8**, 870 (1973).

[14] E.E. Haller, W.L. Hansen, "High resolution fourier transform spectroscopy of shallow acceptors in ultra-pure germanium," Solid State Commun., **15**, 687-692 (1974).

[15] M.S. Skolnick, L. Eaves, R.A. Stradling, J.C. Portal, S. Askenazy, "Far infrared photoconductivity from majority and minority impurities in high purity Si and Ge," Solid State Commun., **15**, 1403-1408 (1974).

[16] V. Aleshkin, L. Gavrilenko, M. Odnoblyudov, I. Yassievich, "Impurity resonance states in semiconductors," Semiconductors, **42**, 880-904 (2008) and references therein.

[17] A.V. Andrianov, A.O. Zakhar'in, I.N. Yassievich, N.N. Zinov'ev, "Terahertz electroluminescence under conditions of shallow acceptor breakdown in germanium," JETP Lett., **79**, 365-367 (2004).

[18] A.V. Andrianov, A. Zakhar'in, I.N. Yassievich, N.N. Zinov'ev, "Linearly polarized terahertz radiation in uniaxially deformed Ge(Ga) upon the electric breakdown of an impurity," JETP Lett., **83**, 351-354 (2006).

[19] A.V. Andrianov, A.O. Zakhar'in, I.N. Yassievich, N.N. Zinov'ev, "Linear polarized terahertz emission under electrical breakdown of a shallow acceptor in uniaxially deformed germanium," Acta Physica Polonica A, **113**, 863-867 (2008).

[20] J.M. Luttinger, W. Kohn, "Motion of Electrons and Holes in Perturbed Periodic Fields," Phys. Rev., **97**, 869 (1955).
[21] S.T. Pantelides, C.T. Sah, "Theory of localized states in semiconductors. I. New results using an old method," Phys. Rev. B, **10**, 621 (1974).
[22] S.T. Pantelides, C.T. Sah, "Theory of localized states in semiconductors. II. The pseudo impurity theory application to shallow and deep donors in silicon," Phys. Rev. B, **10**, 638 (1974).
[23] A. Baldereschi, N.O. Lipari, Interpretation of acceptor spectra in Si and Ge, in: F.G. Fumi (Ed.) Proc. 13th Int. Conf. Phys. Semicond., Tipografia Marves, Rome, 1976, pp. 595.
[24] N.O. Lipari, A. Baldereschi, "Interpretation of acceptor spectra in semiconductors," Solid State Commun., **25**, 665-668 (1978).
[25] N.O. Lipari, A. Baldereschi, M.L.W. Thewalt, "Central cell effects on acceptor spectra in Si and Ge," Solid State Commun., **33**, 277-279 (1980).
[26] R. Buczko, F. Bassani, "Shallow acceptor resonant states in Si and Ge," Phys. Rev. B, **45**, 5838 (1992).
[27] E. Rotsaert, P. Clauws, J. Vennik, L. Van Goethem, "Absorption strengths in the far-IR spectrum of shallow donors and acceptors in germanium," Physica B+C, **146**, 75-79 (1987).
[28] E. Rotsaert, P. Clauws, J. Vennik, L. Van Goethem, "Absorption cross sections in the far-IR spectrum of elemental shallow donors and acceptors in germanium," J. Appl. Phys., **65**, 730-735 (1989).
[29] P. Clauws, J. Broeckx, E. Rotsaert, J. Vennik, "Oscillator strengths of shallow impurity spectra in germanium and silicon," Phys. Rev. B, **38**, 12377 (1988).
[30] B.A. Andreev, E.B. Kozlov, T.M. Lifshits, "Oscillator-Strengths of Optical-Transitions in Shallow Impurities and Impurity Complexes in Silicon and Germanium," Sov. Phys. Semicond., **26**, 522-526 (1992).
[31] B.A. Andreev, E.B. Kozlov, T.M. Lifshits, "Oscillator strengths and linewidths of shallow impurity spectra in Si and Ge," Mater. Sci. Forum, **196-201**, 121-126 (1995).
[32] J. Broeckx, P. Clauws, J. Vennik, "Effective-mass states for prolate and oblate ellipsoid bands," Journal of Physics C: Solid State Physics, **19**, 511-521 (1986).
[33] J. Broeckx, J. Vennik, "Interpretation of acceptor excitation spectra in uniaxially stressed germanium," Phys. Rev. B, **35**, 6165 (1987).
[34] R. Buczko, "Effect of uniaxial stress on shallow acceptor states in silicon and germanium," Nuovo Cimento D, **9**, 669-689 (1987).
[35] D.V. Kozlov, "Optical transitions between acceptor states in uniaxially compressed germanium," JETP Lett., **85**, 208-211 (2007).
[36] G.L. Bir, G.E. Pikus, Symmetry and Strain Induced Effects in Semiconductors, Wiley, New York, 1974.
[37] C.Y.-P. Chao, S.L. Chuang, "Spin-orbit-coupling effects on the valence-band structure of

strained semiconductor quantum wells," Phys. Rev. B, **46**, 4110 (1992).
[38] S.M. Kogan, A.F. Polupanov, "Sum-Rule for Intraband Absorption and Oscillator-Strengths of Optical-Transitions in Shallow Acceptor Impurities in Germanium," Solid State Commun., **27**, 1281-1283 (1978).
[39] J.C. Hensel, K. Suzuki, "Quantum resonances in the valence bands of germanium. II. Cyclotron resonances in uniaxially stressed crystals," Phys. Rev. B, **9**, 4219 (1974).
[40] R.L. Aggarwal, "Stress-Modulated Magnetoreflectance for the Direct Transitions $\Gamma_{25'}^{3/2} \to \Gamma_{2'}$ and $\Gamma_{25'}^{1/2} \to \Gamma_{2'}$ in Germanium," Phys. Rev. B, **2**, 446 (1970).
[41] O. Madelung, Semiconductors: Data Handbook, Springer-Verlag, Berlin, 2004.
[42] R.E.M. Vickers, P. Fisher, C.A. Freeth, "Piezo-spectroscopy of the C line of gallium in germanium," Solid State Commun., **65**, 271-274 (1988).
[43] R.A. Faulkner, "Higher Donor Excited States for Prolate-Spheroid Conduction Bands: A Reevaluation of Silicon and Germanium," Phys. Rev., **184**, 713 (1969).
[44] N. Binggeli, A. Baldereschi, "Prediction of line intensities and interpretation of acceptor spectra in semiconductors," Solid State Commun., **66**, 323-328 (1988).
[45] E.M. Gershenzon, G.N. Gol'tsman, M.L. Kagane, "Energy spectrum of acceptors in germanium and its response to magnetic field," Sov. Phys. JEPT, **45**, 769 (1977).
[46] Y.A. Kurskii, "Shallow-acceptor spectral-line fine structure in germanium," Phys. Rev. B, **48**, 5148 (1993).
[47] S. Rodriguez, P. Fisher, F. Barra, "Spectroscopic Study of the Symmetries and Deformation-Potential Constants of Singly Ionized Zinc in Germanium. Theory," Phys. Rev. B, **5**, 2219 (1972).
[48] A.D. Martin, P. Fisher, C.A. Freeth, E.H. Salib, P.E. Simmonds, "Deformation potential constants of gallium impurity in germanium," Phys. Lett. A, **99**, 391-395 (1983).
[49] D.H. Dickey, J.O. Dimmock, "Excitation spectra of group III impurities in germanium under uniaxial stress," J. Phys. Chem. Solids, **28**, 529-542 (1967).
[50] A.R. Goi, K. Syassen, M. Cardona, "Effect of pressure on the refractive index of Ge and GaAs," Phys. Rev. B, **41**, 10104 (1990).
[51] K.D. Maranowski, A.C. Gossard, K. Unterrainer, E. Gornik, "Far-infrared emission from parabolically graded quantum wells," Appl Phys Lett, **69**, 3522-3524 (1996).
[52] J. Ulrich, R. Zobl, K. Unterrainer, G. Strasser, E. Gornik, K.D. Maranowski, A.C. Gossard, "Temperature dependence of far-infrared electroluminescence in parabolic quantum wells," Appl Phys Lett, **74**, 3158-3160 (1999).
[53] Y. Chassagneux, R. Colombelli, W. Maineult, S. Barbieri, H.E. Beere, D.A. Ritchie, S.P. Khanna, E.H. Linfield, A.G. Davies, "Electrically pumped photonic-crystal terahertz lasers controlled by boundary conditions," Nature, **457**, 174-178 (2009).
[54] Y. Chassagneux, R. Colombelli, W. Maineult, S. Barbieri, S.P. Khanna, E.H. Linfield,

A.G. Davies, "Predictable surface emission patterns in terahertz photonic-crystal quantum cascade lasers," Opt Express, **17**, 9491-9502 (2009).
[55] C.G. Vandewalle, "Band Lineups and Deformation Potentials in the Model-Solid Theory," Phys Rev B, **39**, 1871-1883 (1989).
[56] P. Harrison, Quantum Wells, Wires and Dots: Theoretical and Computational Physics of Semiconductor Nanostructures, Wiley, Chichester, 2005.
[57] P. Lawaetz, "Valence-Band Parameters in Cubic Semiconductors," Phys Rev B, **4**, 3460 (1971).
[58] M. Lundstrom, Fundamentals of Carrier Transport, Cambridge University Press, Cambridge, 2000.
[59] S.L. Chuang, Physics of Optoelectronic Devices, Wiley, New York, 1995.